



Article

CoFe Alloy-Coupled Mo₂C Wrapped by Nitrogen-Doped Carbon as Highly Active Electrocatalysts for Oxygen Reduction/Evolution Reactions

Jiahao Xie ^{1,†}, Yu Miao ^{1,†}, Bin Liu ¹, Siliang Shao ¹, Xu Zhang ¹, Zhiyao Sun ^{1,*}, Xiaoqin Xu ¹, Yuan Yao ^{2,*}, Chaoyue Hu ¹ and Jinlong Zou ^{1,*}

¹ Key Laboratory of Functional Inorganic Material Chemistry, Ministry of Education of the People's Republic of China, School of Chemistry and Materials Science, Heilongjiang University, Harbin 150080, China

² MIIT Key Laboratory of Critical Materials Technology for New Energy Conversion and Storage, School of Chemistry and Chemical Engineering, Harbin Institute of Technology, Harbin 150080, China

* Correspondence: zhiyao202@126.com (Z.S.); yyuan@hit.edu.cn (Y.Y.); zoujinlong@hlju.edu.cn (J.Z.)

† These authors contributed equally to this work.

Abstract: Molybdenum carbide (Mo₂C) with a Pt-like d-band electron structure exhibits certain activities for oxygen reduction and evolution reactions (ORR/OER) in alkaline solutions, but it is questioned due to its poor OER stability. Combining Mo₂C with transition metals alloy is a feasible way to stabilize its electrochemical activity. Herein, CoFe-Prussian blue analogues are used as a precursor to compound with graphitic carbon nitride and Mo⁶⁺ to synthesize FeCo alloy and Mo₂C co-encapsulated N-doped carbon (NG-CoFe/Mo₂C). The morphology of NG-CoFe/Mo₂C (800 °C) shows that CoFe/Mo₂C heterojunctions are well wrapped by N-doped graphitic carbon. Carbon coating not only inhibits growth and agglomeration of Mo₂C/CoFe, but also enhances corrosion resistance of NG-CoFe/Mo₂C. NG-CoFe/Mo₂C (800 °C) exhibits an excellent half-wave potential ($E_{1/2} = 0.880$ V) for ORR. It also obtains a lower OER overpotential (325 mV) than RuO₂ due to the formation of active species (CoOOH/ β -FeOOH, as indicated by in-situ X-ray diffraction tests). $E_{1/2}$ shifts only 6 mV after 5000 ORR cycles, while overpotential for OER increases only 19 mV after 1000 cycles. ORR/OER performances of NG-CoFe/Mo₂C (800 °C) are close to or better than those of many recently reported catalysts. It provides an interfacial engineering strategy to enhance the intrinsic activity and stability of carbides modified by transition-metals alloy for oxygen electrocatalysis.

Keywords: bifunctional electrocatalysts; in-situ X-ray diffraction; Prussian blue analogues; synergistic effect; transition metal carbides



Citation: Xie, J.; Miao, Y.; Liu, B.; Shao, S.; Zhang, X.; Sun, Z.; Xu, X.; Yao, Y.; Hu, C.; Zou, J. CoFe Alloy-Coupled Mo₂C Wrapped by Nitrogen-Doped Carbon as Highly Active Electrocatalysts for Oxygen Reduction/Evolution Reactions. *Nanomaterials* **2023**, *13*, 543. <https://doi.org/10.3390/nano13030543>

Academic Editor: Justo Lobato

Received: 1 January 2023

Revised: 19 January 2023

Accepted: 23 January 2023

Published: 29 January 2023



Copyright: © 2023 by the authors. Licensee MDPI, Basel, Switzerland. This article is an open access article distributed under the terms and conditions of the Creative Commons Attribution (CC BY) license (<https://creativecommons.org/licenses/by/4.0/>).

1. Introduction

The development of renewable energy conversion and storage systems is urgent and necessary in the current society where fossil fuels are in short supply and the environment is severely damaged [1,2]. The electrochemical oxygen reduction and evolution reactions (ORR/OER) are the key half-reactions on the air cathode of energy conversion systems, including metal-air batteries (MABs), direct methanol fuel cells, and hydrogen fuel cells [2,3]. However, the slow kinetics of these two half-reactions limit their large-scale developments for practical application in MABs [1,4]. Currently, Pt-based materials usually exhibit impressive ORR activity, while IrO₂/RuO₂ materials are the main catalysts for OER [5,6]. Unfortunately, the practical use of these noble metal-based catalysts for ORR/OER is hindered by their high cost and low catalytic stability with a high susceptibility to OH⁻ ion poisoning [7,8]. Therefore, the development of cheap, efficient, and stable ORR/OER catalysts for MABs is of great significance for environmental protection and economic development.

Carbon materials doped with non-precious transition metal carbides have proven to be good alternatives to noble metal catalysts by virtue of their low cost and excellent ORR/OER

dual functionality [9]. Among them, molybdenum carbide has received a lot of attention as an active material due to its excellent electrical conductivity, good corrosion resistance, and d-band electronic structure similar to that of Pt group metals [6,10]. For example, Du et al. synthesize the highly stable molybdenum carbide (Mo_2C) nanodots anchored within the 3D carbon nanocages (denoted as $\text{Mo}_2\text{C}/\text{C}$) by pyrolysis of molybdenum tartrate dry gels at high temperatures. $\text{Mo}_2\text{C}/\text{C}$ -0.5 requires only a low overpotential of 164 mV (η_{10}) for HER in 1 M KOH solution [11]. Guo et al. develop a simple method for loading ultrafine Mo_2C nanoparticles onto N-doped carbon nanosheets to obtain mesoporous 2D nanosheets ($\text{MMo}_2\text{C}/\text{NCS}$) with a unique mesoporous nature, which shows an excellent ORR catalytic activity (half-wave potential ($E_{1/2}$) of 0.85 V) [12]. However, the high-temperature calcination not only causes the agglomeration of small particles during the synthesis process, but it also generates the corresponding metallic impurities, which may lead to the formation of large-sized Mo_2C particles and reduce the number of active sites, ultimately lowering the electrocatalytic performance [13].

As reported recently, controlled doping of transition metals (Fe, Co, Ni, etc.) or their alloys with promising electrochemical properties into a nanomaterial can effectively increase its electrical conductivity and catalytic activity [1,8,14]. Kou et al. find that the heterostructures composed of Co-species and Mo_2C together have better OER catalytic properties than those of single Co-based or Mo_2C material [15]. The OER overpotential of Mo_2C catalyst alone is 310 mV, which changes to 190 mV at 10 mA cm^{-2} after the addition of Co species. The excellent OER performance is attributed to the chemical coupling that occurs at the interface between Co-species and Mo_2C , which enhances the electrophilicity and OH^- affinity and forms a hydrated oxide layer on the surface of Co-species [8,15]. Gu et al. synthesize non-precious metal electrocatalysts consisting of Mo_2C nanosheets arranged vertically on the surface of Co@NC. Thanks to the interfacial effect between Co@NC and Mo_2C , $\text{Mo}_2\text{C}/\text{Co@NC}$ exhibits excellent tri-functional electrochemical properties of ORR ($E_{1/2} = 0.86$ V), OER ($\eta_{10} = 308$ mV), and HER ($\eta_{10} = 51$ mV) [1]. Peng et al. report the in-situ synthesis of a $\text{Mo}_2\text{C}/\text{FeNi}$ alloy-combined catalyst with high electrical conductivity (FeNi– $\text{Mo}_2\text{C}/\text{carbon flower}$) by using a hydrothermal method [10]. The unique flower-like porous structure can provide efficient mass transfer pathways to obtain the excellent electrocatalytic performance [10]. Moreover, due to the synergistic effect between geometric design and electronic modification, more active sites on the flower-like structure of the FeNi– $\text{Mo}_2\text{C}/\text{carbon}$ catalyst are exposed, which correspondingly accelerates the electron transfer to enhance the OER activity ($\eta_{10} = 228$ mV) [10]. These studies clearly show that the electrochemical performance of Mo_2C doped with metallic species or alloys is much better than that of the undoped one. Therefore, it is reasonable to combine the Mo_2C with the transition metal alloy to enhance electrochemical performance [15]. However, the ORR/OER dual functions jointly promoted by the composite with Mo_2C and transition metal alloys are still not comprehensive and need to be further investigated.

Herein, we use solid nanospheres (CoFe-Prussian blue analogues/polyvinyl pyrrolidone, CoFe-PBA/PVP), Mo^{6+} , and graphitic carbon nitride ($g\text{-C}_3\text{N}_4$) to prepare a non-precious metal ORR/OER bifunctional electrocatalyst (NG-CoFe/ Mo_2C) by using a simple carbonization method. The catalyst consists of an outer graphitized carbon layer and an inner metal species (CoFe/ Mo_2C). The special structure not only provides abundant electron transfer channels and facilitates the exposure of more active sites, but it also protects the inner metal species from alkaline corrosion to enhance the catalytic stability. The close contact between Mo_2C and CoFe alloy can generate a large number of active sites for ORR/OER. Moreover, N species (originated from $g\text{-C}_3\text{N}_4$) and Mo_2C can jointly act as electron donors for the C atoms in the shell. It is expected that the NG-CoFe/ Mo_2C catalysts should exhibit better catalytic activity and stability than those of commercial Pt/C (ORR) and RuO_2 (OER) in alkaline electrolytes, providing a new perspective on the development of non-precious metal carbide/alloy-based bifunctional electrocatalysts.

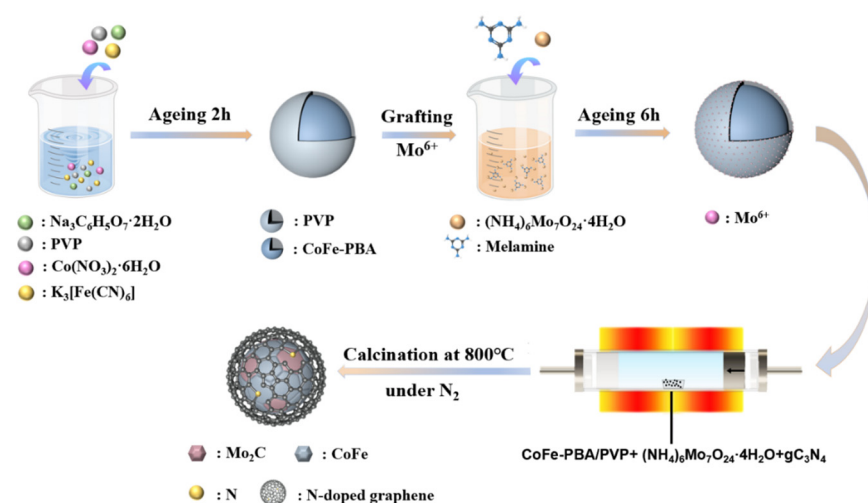
2. Materials and Methods

2.1. Synthesis of CoFe-PBA/PVP and *g*-C₃N₄ Precursors

The CoFe-PBA/PVP hybrid precursor was synthesized by using a co-precipitation method [3,16]. 2.646 g (9 mM) of sodium citrate (Na₃C₆H₅O₇·2H₂O), 1.746 g (6 mM) of cobalt nitrate hexahydrate (Co(NO₃)₂·6H₂O), and 1.2 g of PVP were dissolved in 100 mL of anhydrous ethanol to form a clarified solution (Solution A). A total of 1.317 g of potassium hexacyanoferrate (III) (K₃[Fe(CN)₆]) was dissolved in 40 mL of H₂O to form Solution B, which was then added dropwise to Solution A under magnetic stirring for 5 min. The above mixed solution was aged at room temperature (25 °C) for 2 h. The precipitate was collected by centrifugation and dried at 60 °C for 12 h. For synthesis of *g*-C₃N₄ nanotubes, 5 g of melamine was put into a crucible and heated at 550 °C for 4 h with a heating rate of 5 °C min⁻¹ in a muffle furnace. After cooling naturally to room temperature (25 °C), a yellow solid (*g*-C₃N₄ nanotubes) was obtained and ground into powder for future use [17,18].

2.2. Synthesis of Fe-N/C Catalyst

An amount equal to 0.2 g of the above synthesized Co-Fe PBA/PVP precursor, 0.2 g of (NH₄)₆Mo₇O₂₄·4H₂O, and 0.2 g of *g*-C₃N₄ were dispersed in 20 mL of H₂O, and then the mixture was aged for 6 h at room temperature (25 °C). The dark green precipitate was collected by centrifugation and dried at 60 °C for 12 h (denoted as CoFeMo-CN). As reported previously, Mo⁶⁺ ((NH₄)₆Mo₇O₂₄·4H₂O) was coupled to the CoFe-PBA/PVP precursor by coordination between the pyridine group of PVP and Mo⁶⁺ to form the solid spheres loaded with a large number of Mo⁶⁺ on the surface [14]. The CoFeMo-CN sample was annealed at 700, 750, 800, 850, or 900 °C under N₂ atmosphere for 2 h at a heating rate of 3 °C min⁻¹ to obtain the NG-CoFe/Mo₂C-*x* (*x* = 700, 750, 800, 850, or 900) catalyst. The synthesis process (Scheme 1) had three steps, including template growth, surface attachment, and carbonization. For comparison, the catalyst without (NH₄)₆Mo₇O₂₄·4H₂O was also prepared using the same procedure and denoted as NG-CoFe. Characterization methods for the prepared materials including X-ray diffraction (XRD), Raman spectroscopy, contact angle, X-ray photoelectron spectroscopy (XPS), Fourier Transform Infrared (FTIR) spectroscopy, scanning electron microscopy (SEM), transmission electron microscopy (TEM), energy dispersive x-ray spectroscopy (EDS), and N₂ adsorption/desorption isotherms were described in the ‘Supplementary Materials’.



Scheme 1. Synthesis route for NG-CoFe/Mo₂C-800 composites.

2.3. Electrochemical Measurements

Electrochemical ORR/OER measurements were performed in a three-electrode configuration with a CHI 760 E electrochemical workstation, using a glassy carbon electrode

as the working electrode. A homogeneous ink was prepared by mixing 0.005 g of the synthesized electrocatalyst, 50 μL of nafion, and 100 μL of anhydrous ethanol together under ultrasonication for 0.5 h. The resulting catalyst ink was dropped onto the glassy carbon electrode with an electrocatalyst loading of approximately 0.2 mg cm^{-2} . In this study, commercial Pt/C (10 wt.%) and RuO₂ were used as reference catalysts for ORR and OER, respectively. Among them, commercial Pt/C (10 wt.%, Shanghai Hosen Electric Co., Ltd., Shanghai, China) used VXC72R conductive carbon black as the carbon carrier. Electrochemical tests including cyclic voltammetry (CV), linear scanning voltammetry (LSV), electrochemical impedance spectroscopy (EIS), rotating disk electrode (RDE), rotating ring disk electrode (RRDE), double-layer capacitance (Cdl), electrochemical active surface area (ECSA), transformation frequency (TOF), Faraday efficiency, chronoamperometry (CA), and accelerated durability testing (ADT) were described in the ‘Supplementary Materials’.

3. Results

3.1. Structural and Compositional Analyses

To determine the crystal structure of the NG-CoFe/Mo₂C-x catalysts, powder XRD tests are performed. As shown in Figure 1a, the peaks (NG-CoFe and NG-CoFe/Mo₂C-800) at around 44.9° and 65.4° exactly match the (110) and (200) planes of the CoFe alloy (JCPDS: 49-1568), respectively [19]. The diffraction peaks at $2\theta = 34.3^\circ, 38.0^\circ, 39.4^\circ, 52.1^\circ, 61.5^\circ, 69.7^\circ, 72.4^\circ, 74.7^\circ,$ and 75.5° can be indexed to the (100), (022), (101), (102), (110), (103), (200), (112), and (201) crystalline planes of Mo₂C (JCPDS:35-0787), respectively. It can be observed that all the diffraction peaks of NG-CoFe/Mo₂C-800 match well with those of the CoFe alloy and Mo₂C. The synergies between CoFe alloy and Mo₂C should enhance the electrocatalytic activity of the NG-CoFe/Mo₂C-x catalyst. Specifically, the CoFe alloy can provide a large number of electrons to fill the antibonding orbitals of Mo, which can weaken the O–O bond and further promote the desorption of O-intermediates [20]. Figure 1b exhibits the XRD patterns of the catalysts carbonized at different temperatures. It can be noticed that the diffraction peaks of these catalysts are basically the same as those of NG-CoFe/Mo₂C-800, revealing that the NG-CoFe/Mo₂C-x catalysts are successfully synthesized. In addition, the XRD patterns of NG-CoFe/Mo₂C-x ($x = 700, 750, 800, 850,$ and 900) show the broad diffraction peaks (unobvious) at around 24.3° , corresponding to the (002) plane of the graphitized carbon.

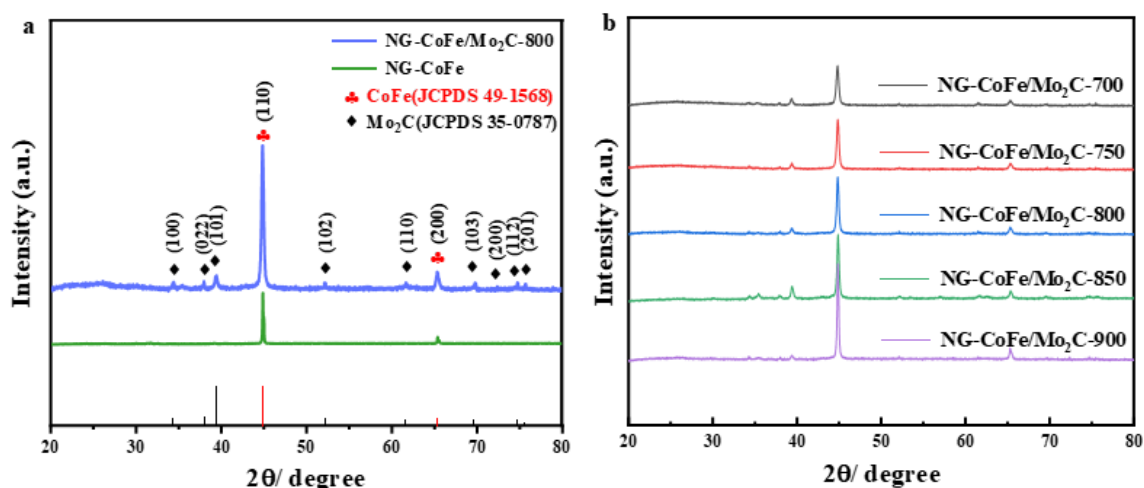


Figure 1. (a) XRD patterns of NG-CoFe and NG-CoFe/Mo₂C-800; (b) XRD patterns of NG-CoFe/Mo₂C-x ($x = 700, 750, 800, 850,$ and 900) catalysts.

To analyze the carbon structure defects of catalysts, Raman tests are performed for NG-CoFe/Mo₂C-x ($x = 700, 750, 800, 850,$ and 900). As shown in Figure 2a, both NG-CoFe/Mo₂C-800 and NG-CoFe materials have two strong peaks at around 1352 and 1578 cm^{-1} , which can be attributed to the D and G bands, respectively. Generally, the

graphitization degree of carbon materials is positively correlated with the I_D/I_G ratio [21]. The I_D/I_G ratio of NG-CoFe/Mo₂C-800 is 0.573, indicating that its carbon skeleton has many defects and a high degree of graphitization. In contrast, the graphitization degree (I_D/I_G ratio of 0.901) of NG-CoFe (without Mo₂C) is higher than that of NG-CoFe/Mo₂C-800. It indicates that the incorporation of the Mo-species generates a large number of defects in the carbon lattice, which may significantly enhance the ORR activity [22]. The changes in the surface groups of NG-CoFe/Mo₂C-800 before and after carbonization are further analyzed by FT-IR spectroscopy (Figure 2b). For the pre-fired CoFeMo-CN sample, the peaks at around 589, 1572, 1635, and 2085 cm⁻¹ are caused by the stretching vibrations of Fe–C bond, the bending vibration of C–C bond, the resonance vibration of C=C bond, and the vibration of –C≡N– bond, respectively [23,24]. In addition, the NG-CoFe/Mo₂C-800 catalyst mainly has two carbon characteristic vibrations at around 1556 and 2085 cm⁻¹, which correspond to the stretching vibrations of C–N and –C≡N–, respectively [25]. According to the comparison, it can be found that the –C≡N– bond continues to exist before and after the calcination, while the C–N bond is newly generated, indicating that some of the –C≡N– bonds may be broken and converted into C–N bonds at high temperatures [25].

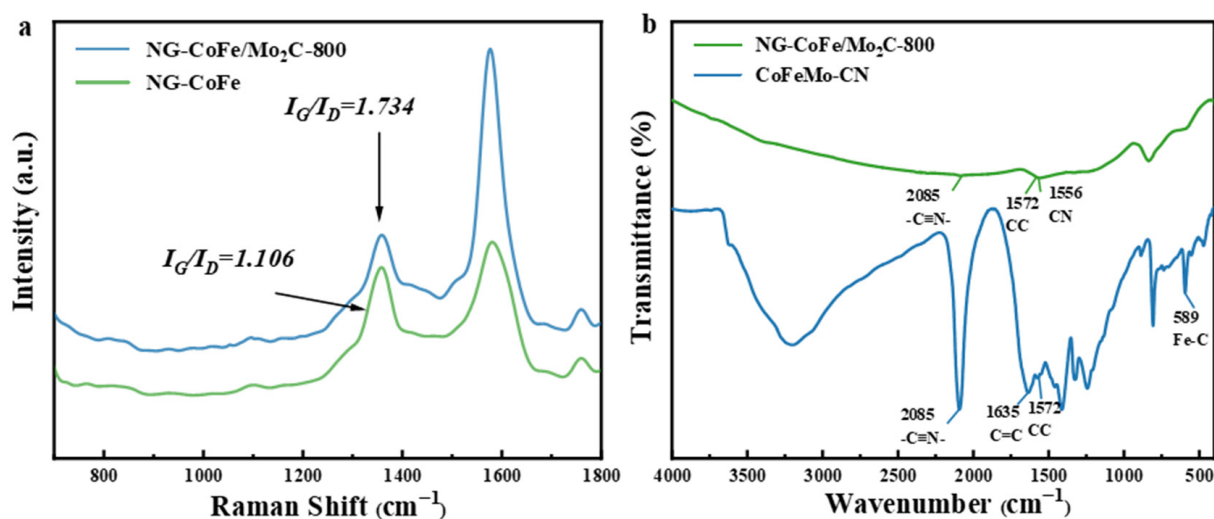


Figure 2. (a) Raman spectra of NG-CoFe/Mo₂C-800 and NG-CoFe; (b) FTIR spectra of NG-CoFe/Mo₂C-800 and CoFeMo-CN.

The electrocatalytic properties are closely related to the valence electronic states of elements on the surface of the catalyst [26]. As shown in the XPS survey spectra (Figure 3a), all of the NG-CoFe/Mo₂C-x catalysts consist of six elements including C, N, O, Fe, Co, and Mo. Among them, the existence of oxygen species may be ascribed to the introduction of a small amount of air during the carbonization process. The percentage contents (wt.%) of C 1s, N 1s, O 1s, Co 2p, Fe 2p, and Mo 3d in NG-CoFe/Mo₂C-x are shown in Table S1. The C 1s peak of NG-CoFe/Mo₂C-800 can be deconvoluted into two peaks of 284.6 eV (C–C) and 285.5 eV (C–N) (Figure 3b). The presence of C–N bond can also indicate the successful doping of N atoms into the carbon skeleton [14]. Figure 3c shows the N 1s spectrum of NG-CoFe/Mo₂C-800, which can be divided into three peaks including 398.4 (pyridine N), 399.8 (pyrrole N) and 401.1 eV (graphitic N). It is expected that the N species in the catalyst can enhance the ORR activity. Generally, pyrrole N can accelerate the breaking of the O–O bond and the oxygen trapping [27]. Pyridine N can provide a large number of defects and increase the spin density of C atoms, while graphitic N facilitates charge transfer to enhance ORR activity [27].

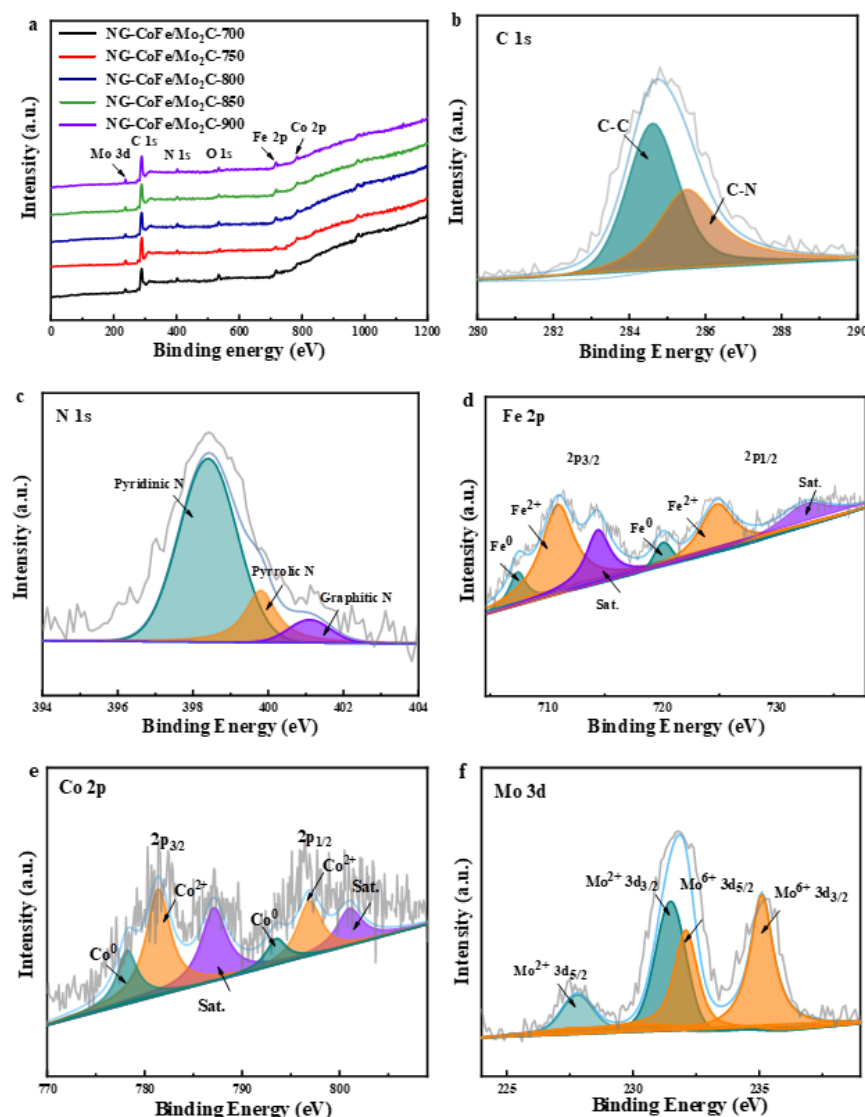


Figure 3. XPS survey spectra (a) for NG-CoFe/Mo₂C-x and high-resolution XPS spectra of C 1s (b), N 1s (c), Fe 2p (d), Co 2p (e), and Mo 3d (f) for NG-CoFe/Mo₂C-800.

As shown in Figure 3d, the high-resolution spectrum of Fe 2p can be deconvoluted into six peaks of 707.4, 720.1, 710.9, 724.8, 714.4, and 732.5 eV. The peaks at 707.4 and 720.1 eV correspond to Fe⁰, while the peaks at 710.9 and 724.8 eV correspond to Fe²⁺ [28]. The Fe 2p band located at around 714.4 and 732.5 eV are attributed to the satellite peaks. The presence of Fe⁰ indicates the successful synthesis of FeCo alloys under high-temperature pyrolysis conditions, while the infiltration of oxygen during carbonization is responsible for the appearance of Fe²⁺ (the oxidation of Fe⁰ by O₂) [28]. In Figure 3e, the high-resolution spectrum of Co 2p can be divided into six peaks. The binding energies of 778.2 and 793.5 eV correspond to Co⁰ of the 2p_{3/2} and 2p_{1/2} orbitals, respectively, while the peaks at around 781.4 and 796.9 eV are assigned to the 2p_{3/2} and 2p_{1/2} spin orbitals of Co²⁺ [29]. In addition, the peaks around 787.1 and 801.1 eV are satellite peaks, further revealing the formation of CoFe alloys in the composite [27,30,31]. The change in binding energy may be due to the establishment of a new equilibrium of the charge distribution between CoFe and Mo₂C. In Figure 3f, the high-resolution spectrum of Mo 3d is divided into two pairs of peaks with binding energies of 227.8/231.5 and 232.1/235.1 eV, corresponding to Mo²⁺ and Mo⁶⁺, respectively [32]. The presence of Mo⁶⁺ is attributed to the surface oxidation of Mo₂C, which is consistent with previous study [33]. The XPS results demonstrate the successful synthesis of the complex structure (Mo₂C coupled with FeCo alloy). The high-resolution

XPS spectra of NG-CoFe/Mo₂C-*x* (*x* = 700, 750, 850, and 900) catalysts with C 1s, N 1s, Fe 2p, Co 2p, and Mo 3d are shown in Figures S1–S4.

As shown in Figure 4a, the FESEM image of the CoFe-PBA/PVP hybrid precursor shows a spherical structure with a particle diameter of approximately 20 nm. The PVP layer covering the surface can effectively prevent the agglomeration of CoFe-PBA. After doping with Mo⁶⁺ and g-C₃N₄ (Figure 4b), the regular solid spheres become irregular aggregates. After carbonization, the small nanoparticles are stacked together to form a complex structure with a high level of porosity (Figure 4c). The morphology change during the carbonization process may be due to the effect of surface tension generated by the volatilization of residual solvents [30]. As shown in Figure 4d–g, the morphologies of NG-CoFe/Mo₂C-*x* show the bamboo-like nanotube structures after carbonization at different temperatures. The stacked pores (porous structure) of NG-CoFe/Mo₂C-*x* can increase the number of catalytic active sites and mass transfer channels, which should correspondingly enhance the ORR/OER performance [34]. Furthermore, as shown in Figure 4h–n, EDS element mapping images show the presence of five elements including C, N, Fe, Co, and Mo on the surface of NG-CoFe/Mo₂C-800, demonstrating the successful combination of the CoFe alloy and Mo₂C.

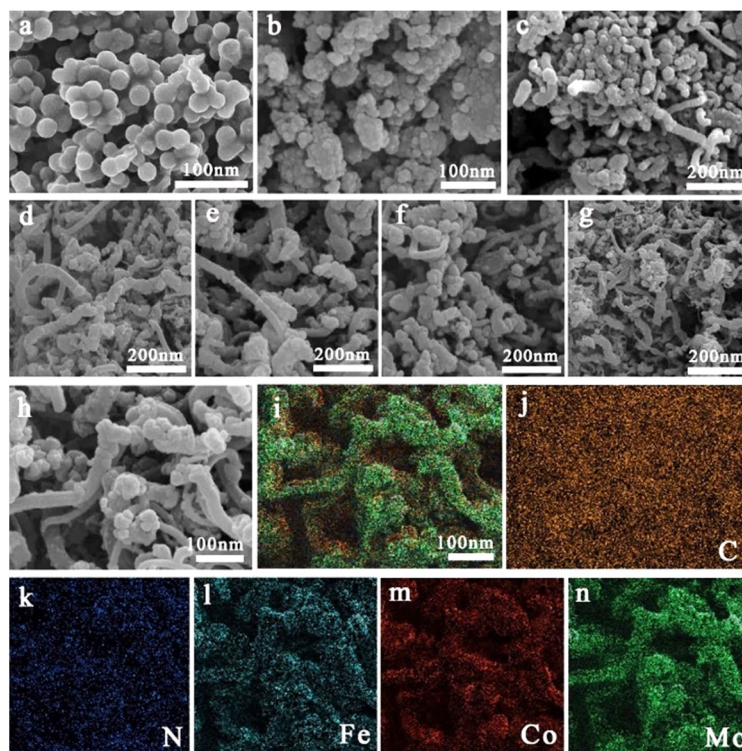


Figure 4. (a) SEM images of CoFePBA/PVP; (b) CoFeMo-CN; (c) NG-CoFe/Mo₂C-800; (d–g) NG-CoFe/Mo₂C-*x* (*x* = 700, 750, 850, or 900); (h) NG-CoFe/Mo₂C-800. Elemental mapping images of NG-CoFe/Mo₂C-800 (i), C (j), N (k), Fe (l), Co (m), and Mo (n) elements.

The nanostructure of NG-CoFe/Mo₂C-800 is further evaluated using TEM images. Many sub-spherical structured particles marked with red circles can be seen in Figure 5a. Most of the Mo₂C particles and CoFe alloys are encapsulated in a robust carbon shell (Figure 5b). Figure 5c clearly shows the lattice stripes with spacing of 0.18, 0.20, and 0.34 nm, which correspond to the (102) crystal plane of Mo₂C, the (110) crystal plane of CoFe alloy, and the (002) crystal plane of graphitized carbon, respectively. It proves the successful synthesis of Mo₂C and CoFe alloy embedded in the carbon skeleton. The presence of graphitized carbon not only effectively facilitates the charge transfer among Mo₂C, CoFe alloy, and carbon during electrocatalysis, but it also reduces the corrosion of Mo₂C and CoFe alloy by the electrolyte and improves the stability of the catalyst [6]. Moreover, the

close contact of CoFe alloys and Mo₂C nanoparticles can improve the electron transfer from the CoFe/Mo₂C nanoparticles to the carbon matrix, which in turn enhances the catalytic performance [35]. As shown in Figure 5d, the selected area electron diffraction (SAED) also reveals the successful synthesis of Mo₂C and FeCo alloy in the graphitized carbon structure, consistent with the HRTEM results.

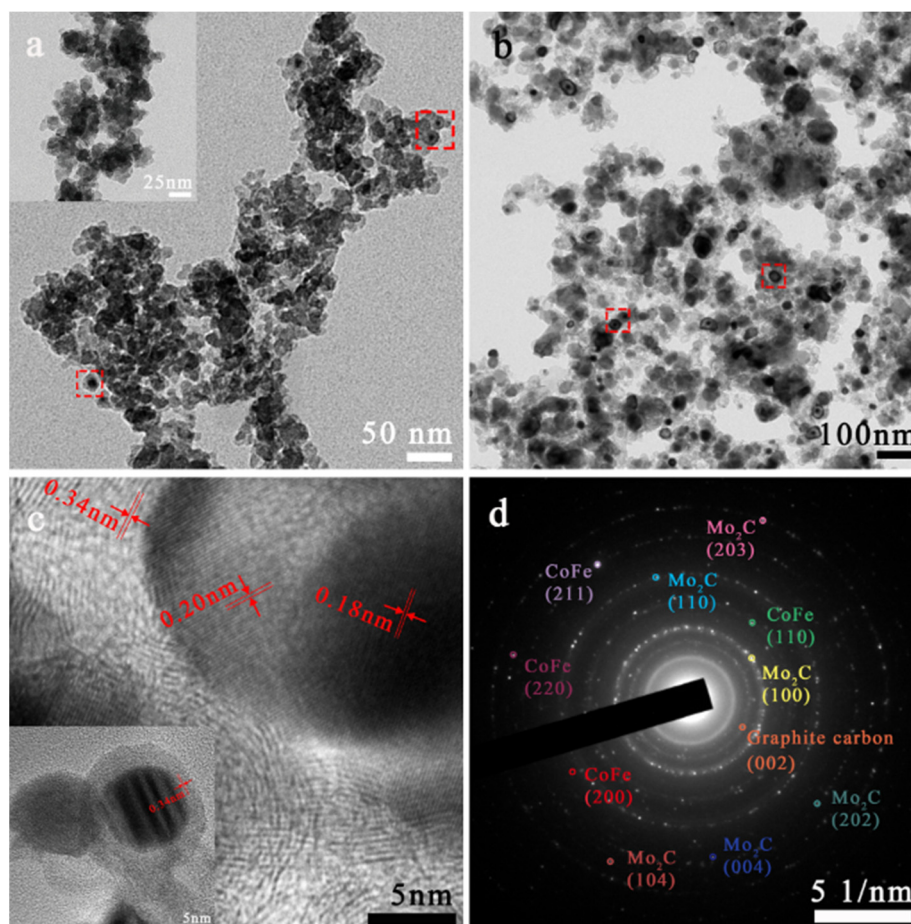


Figure 5. (a) TEM images of CoFeMo-CN; (b) TEM and (c) HRTEM images of NG-CoFe/Mo₂C-800; (d) SAED pattern of NG-CoFe/Mo₂C-800.

N₂ adsorption–desorption isotherms and pore size distribution curves for CoFePBA/PVP, NG-CoFe, and NG-CoFe/Mo₂C-800 are displayed in Figure 6a–c. The specific surface areas (SSAs) of NG-CoFe/Mo₂C-800 are 322.03 m² g^{−1}, which is much higher than those of CoFePBA/PVP (145.74 m² g^{−1}) and NG-CoFe (178.57 m² g^{−1}), respectively (Table S2). The N₂ adsorption–desorption isotherms of these catalysts reveal the typical type IV isotherms with a (mainly) mesoporous characteristic. It reveals that the carbon skeleton is highly porous, which should facilitate the mass (oxygen-related substances) diffusion via the internal pore channels and the exposure of abundant active sites, thus accelerating the ORR/OER kinetics. As indicated previously, the metal cores and porous carbon structure can together enhance the electrocatalytic activity [28]. In order to study the wettability of the catalysts, contact angle measurements are performed. Figure 6d–f show that the contact angles of CoFePBA/PVP, NG-CoFe, and NG-CoFe/Mo₂C-800 are 15.46°, 13.65°, and 8.96°, respectively. The hydrophilic property of NG-CoFe/Mo₂C-800 should be promoted by embedding the hydrophilic CoFe alloy/surface oxides in the carbon skeleton. Moreover, the large surface area with abundant mesopores is also responsible for the better wettability. It indicates that the NG-CoFe/Mo₂C-800 catalyst with a hydrophilic surface facilitates full contact with the electrolyte. It is reported that high wettability can theoretically improve

the adsorption of reactants or products on the catalytic interface, thus improving the electrocatalytic activity [36].

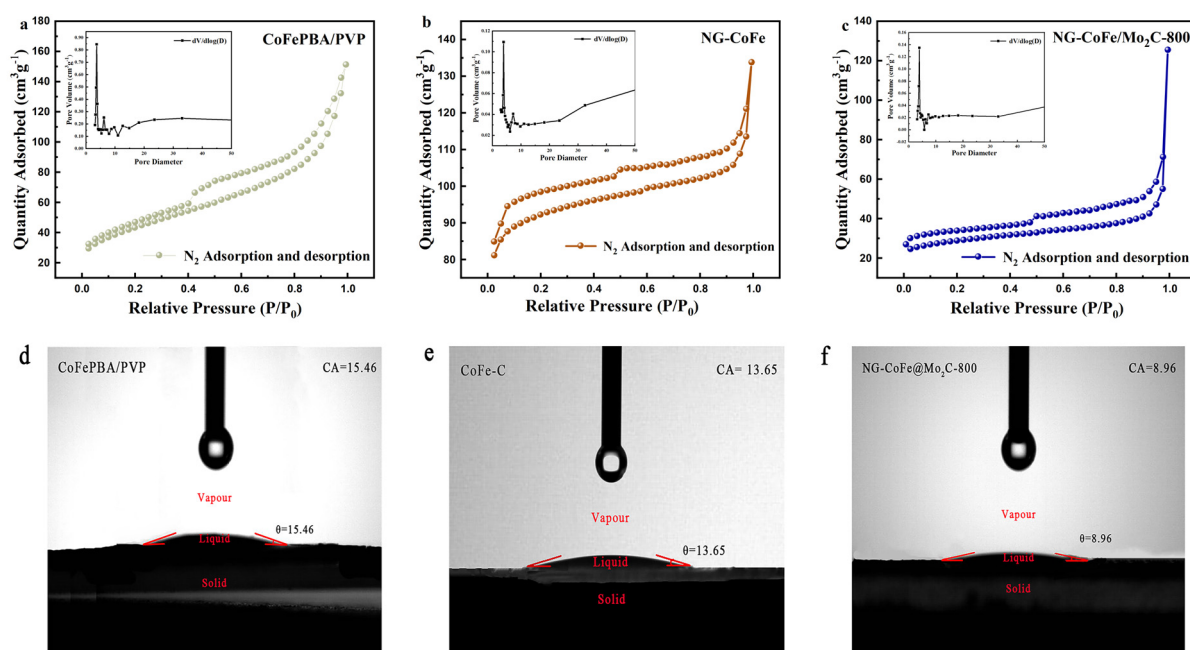


Figure 6. N_2 adsorption/desorption isotherms and pore size distributions (inset) for CoFePBA/PVP (a); NG-CoFe (b); NG-CoFe/ Mo_2C -800 (c). Contact angles of CoFePBA/PVP (d); NG-CoFe (e); NG-CoFe/ Mo_2C -800 (f).

3.2. Electrocatalytic Activities of NG-CoFe/ Mo_2C -x Catalysts for ORR

The ORR activities of NG-CoFe/ Mo_2C -x are evaluated using CV tests in oxygen-saturated 0.1 M KOH electrolyte [37]. In Figure 7a, NG-CoFe/ Mo_2C -800 has an obvious reduction peak at 0.880 V, which is higher than those of commercial 10 wt.% Pt/C (0.830 V) and NG-CoFe (0.802 V). It suggests that the excellent ORR activity is mainly due to the synergies among Mo_2C and CoFe, which can promote the capture of the first electron and accelerate the cleavage of the O=O bond, leading to a significant reduction of the activation potential of the adsorbed O_2 , thus enhancing the ORR activity [38–40]. As reported previously, Mo_2C with a strong negative electronic property has a similar d-band structure to Pt-group metals, which makes it have promising catalytic properties for ORR [37,38]. N dopants (especially pyridine-N) can form the Lewis bases on the adjacent carbon to accelerate the adsorption of oxygen molecules to further enhance the ORR efficiency [12]. In Figure 7b, the reduction peaks of NG-CoFe/ Mo_2C -x (x = 700, 750, 850, and 900) appear at 0.866, 0.856, 0.845, and 0.831, respectively. It reveals that the NG-CoFe/ Mo_2C -800 catalyst has the highest ORR catalytic activity (0.880 V). To gain deeper insight into the ORR dynamics, LSV tests of NG-CoFe/ Mo_2C -x catalysts are conducted in an O_2 -saturated 0.1 M KOH solution at 1600 rpm. In Figure 7c, NG-CoFe/ Mo_2C -800 exhibits the highest ORR activity with a promising $E_{1/2}$ of 0.880 V, which is 50 and 78 mV higher than those of Pt/C (0.830 V) and NG-CoFe (0.802 V), respectively. In Figure 7d, the activity of NG-CoFe/ Mo_2C -800 is superior to other as-prepared catalysts, indicating that more available active sites are exposed on NG-CoFe/ Mo_2C -800 to accelerate the ORR process [41,42]. As reported by our group, the surface Co^{2+} species with neighboring oxygen vacancy can be considered as the active sites, which can promote the adsorption and activation of O_2 for ORR [35,36]. Moreover, Co^{2+} can also transfer electrons to the O_2 absorbed on the active site, thus weakening and breaking the O–O bond to facilitate the ORR process on the surface of NG-CoFe/ Mo_2C -800 [35,36].

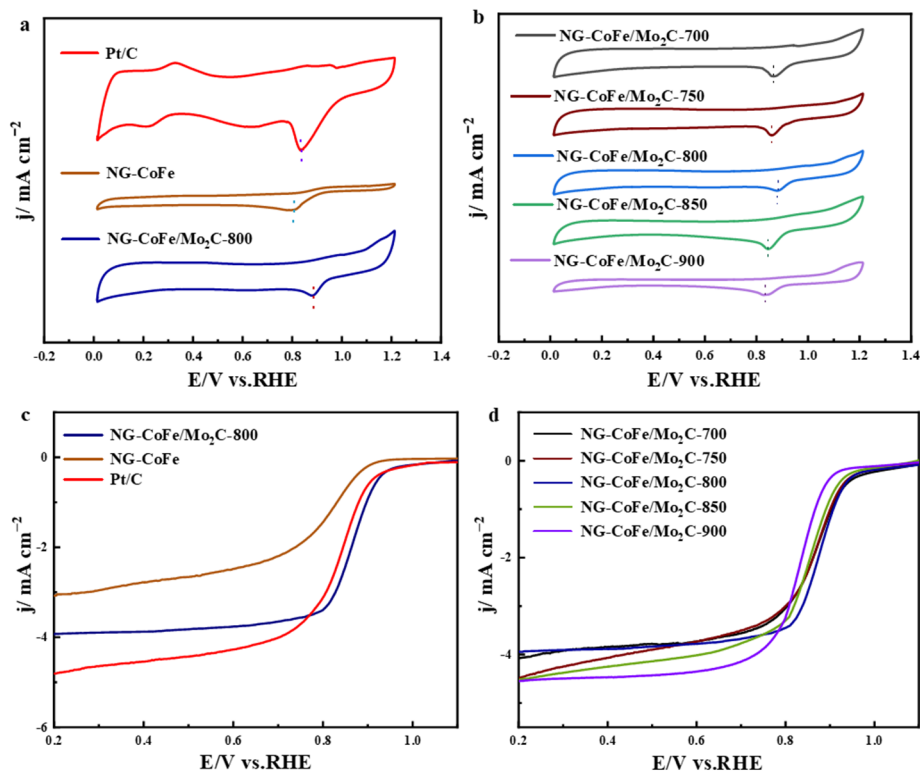


Figure 7. (a) CV curves for NG-CoFe/Mo₂C-800, NG-CoFe, and Pt/C; (b) CV curves for NG-CoFe/Mo₂C-*x* (*x* = 700, 750, 850, and 900) in an O₂-saturated 0.1 M KOH solution at a scan rate of 10 mV s⁻¹; (c) LSV curves for NG-CoFe/Mo₂C-800, NG-CoFe, and Pt/C; (d) LSV for NG-CoFe/Mo₂C-*x* (*x* = 700, 750, 850, and 900) curves (5 mV s⁻¹ and 1600 rpm) in an O₂-saturated 0.1 M KOH solution.

As shown in Figure 8a, the kinetic current density (J_k) of the NG-CoFe/Mo₂C-800 catalyst is 3.1 mA cm⁻² at 0.82 V, which is 2.82 times higher than that of NG-CoFe (1.1 mA cm⁻²) and 1.19 times higher than that of commercial Pt/C (2.6 mA cm⁻²). To summarize, NG-CoFe/Mo₂C-800 catalyst has the highest kinetic current density, further illustrating its favorable catalytic performance [43]. The lower Tafel slope usually confirms the more promising ORR kinetics of the catalyst [44]. Figure 8b shows the Tafel plots of NG-CoFe/Mo₂C-800 and Pt/C. The Tafel slope of NG-CoFe/Mo₂C-800 (92.47 mV dec⁻¹) is better than that of commercial Pt/C (241.16 mV dec⁻¹), indicating that NG-CoFe/Mo₂C-800 catalyst has the faster reaction kinetics. By comparing with NG-CoFe, the superior catalytic performance of NG-CoFe/Mo₂C-*x* should be ascribed to the incorporation of Mo₂C with the electrocatalytic synergies among CoFe alloy, N-doped carbon, and Mo₂C [45,46]. As shown in Figure 8c, the charge transfer resistance (R_{CT}) values of NG-CoFe/Mo₂C-800, NG-CoFe, and Pt/C are 17.73, 56.92, and 64.12 Ω, respectively. Moreover, the R_{CT} values of NG-CoFe/Mo₂C-*x* (*x* = 700, 750, 850, and 900) are 34.01, 42.98, 18.65, and 28.26 Ω, respectively (Figure S5). The lower the R_{CT} and the faster the charge transfer rate of the catalyst [47]. It clearly shows that NG-CoFe/Mo₂C-800 has a faster electron transfer kinetics (Figure S5). These results verify that the introduction of Mo₂C can improve the electronic conductivity to thus promote the charge transfer ability of NG-CoFe/Mo₂C-800 [47]. As deduced, the smooth charge transfer between metal species (Mo₂C and CoFe) with high surface activities and a carbon skeleton (electron-accepting) can be partly attributed to the electron-donating effects of Mo₂C and CoFe, which eagerly induces a charge-transfer from Mo₂C/CoFe to carbon.

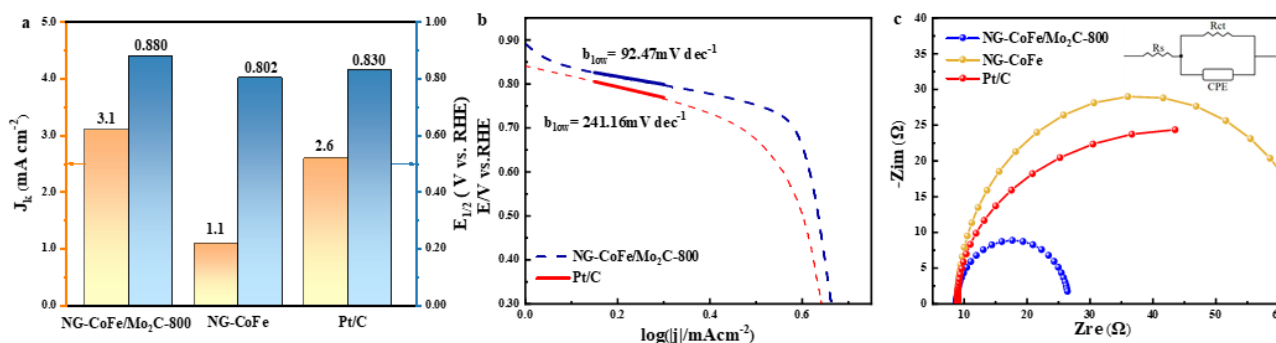


Figure 8. (a) Kinetic current density (J_k) at 0.82 V versus reversible hydrogen electrode (versus RHE) and half-wave potentials of NG-CoFe/Mo₂C-800, NG-CoFe, and Pt/C catalysts; (b) Tafel plots of the NG-CoFe/Mo₂C-800 and Pt/C; (c) Nyquist curves of NG-CoFe/Mo₂C-800, NG-CoFe, and Pt/C in an O₂-saturated 0.1 M KOH solution at a scan rate of 5 mV s⁻¹ with a rotation rate of 1600 rpm.

The ORR kinetics of NG-CoFe/Mo₂C-800 and Pt/C are investigated at different rotational rates (Figure 9a,b). The corresponding Koutecky-Levich (K-L) plots from LSV curves are shown in the insets of Figure 9a,b, and the average number of transferred electrons (n) is calculated based on the slope of the K-L plot (Figure S6). The K-L plots of NG-CoFe/Mo₂C-800 and Pt/C nearly overlap in the potential range of 0.3 to 0.6 V. All curves show excellent linear parallelism with n close to the theoretical value of 4.0, indicating that the catalyst facilitates the 4e⁻ reduction pathway for oxygen [48]. As shown in Figure 9c,d, the H₂O₂ yields and the number of transferred electrons (n) in alkaline electrolytes can be calculated by using the RRDE tests. The H₂O₂ yields of NG-CoFe/Mo₂C-800, NG-CoFe, and Pt/C are between 10.4 and 13.4%, indicating that the NG-CoFe/Mo₂C-800 catalyst has an efficient selectivity for the generation of H₂O, further confirming the 4e⁻ ORR process (mainly) [49]. As shown in Figure 9e, the stability tests are performed in an O₂-saturated 0.1 M KOH solution for 30,000 s of continuous testing. The retention of the current density of the NG-CoFe/Mo₂C-800 catalyst (84.74%) is higher than that of Pt/C (58.30%), and the loss of current density can be partly attributed to the oxidation of metal species during the electrocatalytic process [50]. It is obvious that the NG-CoFe/Mo₂C-800 catalyst has better stability, which may be due to the special structure with CoFe and Mo₂C encapsulated (protected) by the N-doped carbon [51].

As shown in Figure 9f, the current density of Pt/C changes drastically at 300 s when 3 mL of methanol is added to the electrolyte for the CA test, while the curve of the NG-CoFe/Mo₂C-800 catalyst does not show any fluctuation. The excellent methanol resistance of NG-CoFe/Mo₂C-800 is probably due to the large surface area of the carbon matrix, where OH⁻ can be effectively adsorbed to enhance the methanol tolerance during ORR [26]. In addition, the N-doped carbon matrix allows for the particle-wrapped configuration and helps to prevent the aggregation of Mo₂C and CoFe nanoparticles, which in turn enhances the catalytic and structural stabilities of the catalyst [12]. In the accelerated durability tests (ADTs) (Figure S7a,b), the $E_{1/2}$ of NG-CoFe/Mo₂C-800 has a slight shift of 6 mV after 5000 cycles, which is lower than that of Pt/C (15 mV). It indicates that NG-CoFe/Mo₂C-800 can be considered as an excellent ORR electrocatalyst with high catalytic stability and methanol resistance. These promising properties of NG-CoFe/Mo₂C-800 are mainly attributed to its special structure and components, which not only provide sufficient active sites by coupling N-doped carbon with Mo₂C and CoFe nanoparticles, but also provide multiple pathways for the efficient transport of oxygen molecules and electrolytes [10].

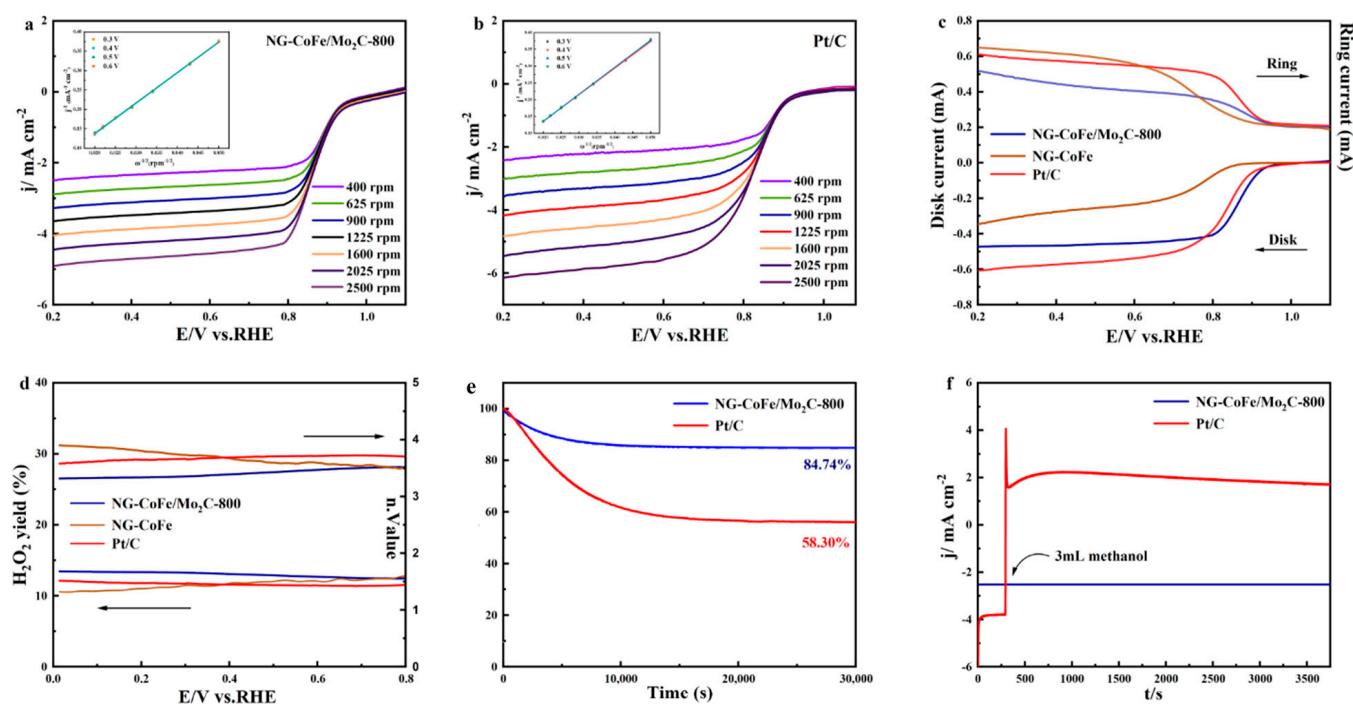


Figure 9. (a) LSV curves and calculated K-L plots (inset) at different potentials of NG-CoFe/Mo₂C-800 and Pt/C (b) in an O₂-saturated 0.1 M KOH at different RDE rotation rates (5 mV s⁻¹); (c) RRDE voltammograms of Pt/C, NG-CoFe and NG-CoFe/Mo₂C-800 in an O₂-saturated 0.1 M KOH solution; (d) H₂O₂ yields and the corresponding electron transfer number (n); (e) chronoamperometric (i-t) responses of NG-CoFe/Mo₂C-800 and Pt/C before and after (f) the addition of 3 mL of methanol in an O₂-saturated 0.1 M KOH at 1600 rpm.

3.3. Electrocatalytic Activities of NG-CoFe/Mo₂C-*x* Catalysts for OER

Figure 10a shows that NG-CoFe/Mo₂C-800 can achieve a current density of 10 mA cm⁻² at an overpotential of 325 mV for OER, which is much smaller (better) than those of NG-CoFe (422 mV) and RuO₂ (389 mV). The OER overpotentials ($E_j = 10$) for NG-CoFe/Mo₂C-*x* (*x* = 700, 750, 800, 850, and 900) catalysts are 351, 341, 343, and 339 mV (Figure S8), respectively. It also indicates that CoFe alloy alone provides a limited OER activity for the NG-CoFe catalyst, while the catalyst with Mo₂C provides a promising OER performance [52–54]. It is reported that the strong interactions between the two elements (Co and Fe) can effectively improve the electrocatalytic activity of alloys for OER [55,56]. The close contact between Mo₂C and CoFe (heterojunction) should lead to the modification of the structure of CoFe alloy, contributing to the formation of highly active CoOOH/FeOOH [57,58]. Moreover, although the protecting role of NG can delay the oxidation of metallic species, the formation of ionic states (Co²⁺/Fe²⁺) of Co/Fe is inevitable, which can effectively accelerate the formation of the key active species (CoOOH/FeOOH) for OER [59]. The catalytic activity is mainly due to the synergistic effect of the heterogeneous structure (CoOOH/FeOOH) formed by the reaction at the three-phase interface [60]. Specifically, the interaction between CoFe and Mo₂C also accelerates the electron transfer rate, enhances the electrophilic effect of Co ions and Fe ions, and strengthens the adsorption capacity for OH⁻, hence increasing the OER activity [60]. To further investigate the OER performance of the catalysts, the corresponding Tafel slopes are obtained from the LSV curves. The Tafel slope is the size of the overpotential required for a 10-fold increase in the exchange current, thus, the smaller the slope, the faster the OER dynamics [52]. In Figure 10b, the Tafel slope of NG-CoFe/Mo₂C-800 (75.49 mV dec⁻¹) is much smaller than that of RuO₂ (173.03 mV dec⁻¹). The Tafel slopes of NG-CoFe/Mo₂C-*x* (*x* = 700, 750, 850, and 900) are 76.39, 86.29, 76.39, and 74.87 mV dec⁻¹, respectively. It shows that NG-CoFe/Mo₂C-800 has a better OER catalytic kinetics [61,62]. In Figure 10c (EIS curve), NG-CoFe/Mo₂C-800

has a smaller R_{CT} (18.33Ω) than those of NG-CoFe (46.75Ω) and RuO_2 (25.94Ω). The active species (CoOOH/FeOOH)-wrapped configuration of NG-CoFe/ Mo_2C -800 may play important roles in enhancing the charge transfer during OER [63–65]. In addition, the N-doped carbon skeleton substantially improves the electrical conductivity, provides high surface area to contact with electrolytes, and disperses the generated CoOOH/FeOOH species without aggregation [66,67].

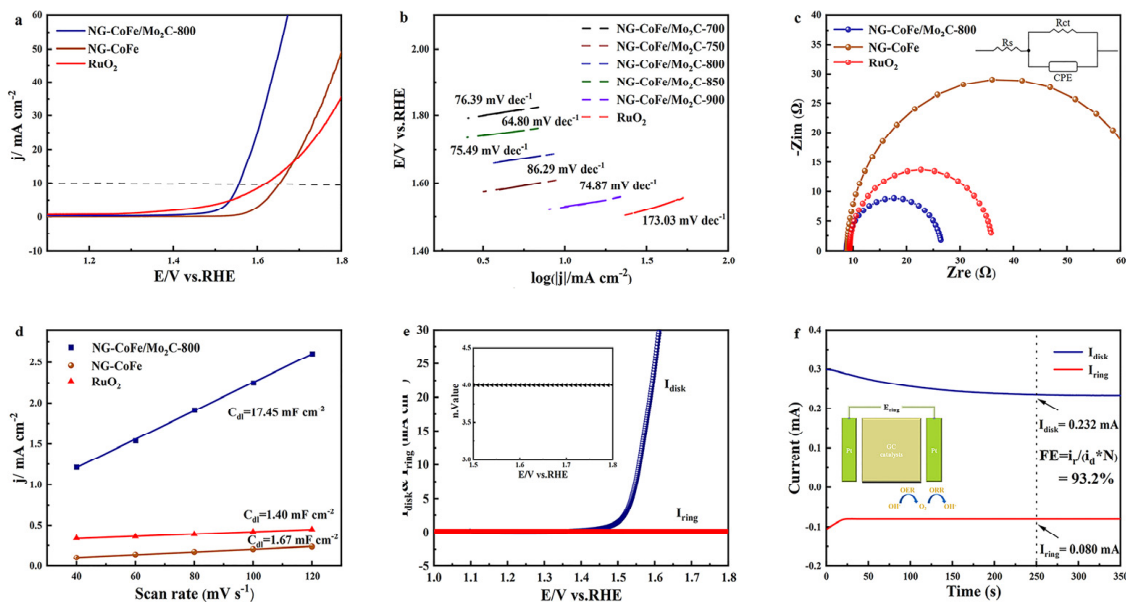


Figure 10. (a) LSV curves of NG-CoFe/ Mo_2C -800, NG-CoFe, and RuO_2 in a 1 M KOH solution for OER (2 mV s^{-1} and 1600 rpm); (b) Tafel plots of NG-CoFe/ Mo_2C -x (700, 750, 800, 850, and 900) and RuO_2 ; (c) Nyquist curves of NG-CoFe/ Mo_2C -800, NG-CoFe and RuO_2 (5 mV s^{-1} and 1600 rpm); (d) linear plots of scan rates vs. current density for NG-CoFe/ Mo_2C -800, NG-CoFe, and RuO_2 in 0.1 M KOH electrolyte; (e) Voltammogram obtained for NG-CoFe/ Mo_2C -800 in 0.1 M KOH on a RRDE (1600 rpm) device; (f) Faradaic efficiency of NG-CoFe/ Mo_2C -800 on a RRDE (1600 rpm) device in a 0.1 M KOH solution (ring potential of 0.4 V vs. RHE).

It is well known that the ECSA can be used to indicate the number of active sites exposed by the catalyst and also to reflect OER catalytic activity [68,69]. ECSA is evaluated using cyclic voltammetry based on CV curves at different scan rates to calculate the double-layer capacitance (C_{dl}) values (Figure 10d and Figure S9). As shown in Figure 10d, the C_{dl} value of NG-CoFe/ Mo_2C -800 (17.45 mF cm^{-2}) is the larger than those of NG-CoFe (1.67 mF cm^{-2}) and RuO_2 (1.40 mF cm^{-2}). The ECSAs of NG-CoFe/ Mo_2C -800, NG-CoFe, and RuO_2 are 436.25, 41.75, and 35.00 mF, respectively. In agreement with the LSV (OER) results, the ECSA of NG-CoFe/ Mo_2C -800 is larger than those of NG-CoFe and RuO_2 . In Figure 10e, the electron transfer number (n) is calculated using RRDE, and n is approximately 4.0 for NG-CoFe/ Mo_2C -800. It shows that the dominant OER pathway is the $4e^-$ transfer process ($4\text{OH}^- \rightarrow 2\text{H}_2\text{O} + \text{O}_2 + 4e^-$) [67,70]. As shown in Figure S10, the turnover frequency (TOF) value calculated for NG-CoFe/ Mo_2C -800 (0.790 s^{-1}) at 10 mA cm^{-2} is superior to that of RuO_2 (0.354 s^{-1}). As shown in Figure 10f, the Faraday efficiency (93.2%) of NG-CoFe/ Mo_2C -800 is obtained by performing the RRDE test, further validating the $4e^-$ pathway for OER and also demonstrating that NG-CoFe/ Mo_2C -800 has an excellent capability for energy conversion [71,72].

Previous studies have mentioned that Mo_2C can significantly improve the OER performance of the catalyst, but it is questioned due to its poor stability [20,54]. Specifically, Mo is easily oxidated to Mo-based oxides during OER, resulting in its poor stability [20]. To investigate the OER stability of NG-CoFe/ Mo_2C -800, continuous LSV measurements are performed (Figure 11a). The overpotential in the LSV curve increases by only 19 mV com-

pared to the initial one after 1000 cycles, and finally the current density is retained by 91.8% (inset of Figure 11a). In Figure 11b, the crystalline phase change of NG-CoFe/Mo₂C-800 is tested during OER by using the in situ XRD technique. The diffraction peaks at around 20.24° and 50.58° correspond to the (0 0 3) and (0 1 5) lattice of CoOOH (JCPDS No. 07-0169), respectively [73]. In addition, the diffraction peaks at around 26.70° and 55.90° correspond to the (3 1 0) and (5 2 1) lattices of β-FeOOH (JCPDS No. 34-1266), respectively [63]. These new active components (CoOOH/FeOOH) should be produced by the oxidation of the Co/Fe species during OER. As reported previously, CoOOH and FeOOH are the main active substances for OER [71,73]. Usually, the value of overvoltage ($\Delta E = E_{j=10} - E_{1/2}$) is used to evaluate efficiency loss, which can validly indicate the bifunctional electrocatalytic activity of the catalyst [49]. A smaller ΔE value indicates a lower efficiency loss and higher catalytic activity as a reversible oxygen electrode [67,74]. The as-prepared NG-CoFe/Mo₂C-800 catalyst exhibits excellent catalytic activity with a ΔE of 0.67 V (Figure 11c). As shown in Figure S11, the NG-CoFe/Mo₂C-800 catalyst almost maintains its original morphology after the stability tests of ORR and OER. In Figure 11d, the ORR and OER activities of the NG-CoFe/Mo₂C-800 are compared with those of bifunctional electrocatalysts in the literature, which further illustrates that NG-CoFe/Mo₂C-800 can be considered an efficient ORR/OER catalyst.

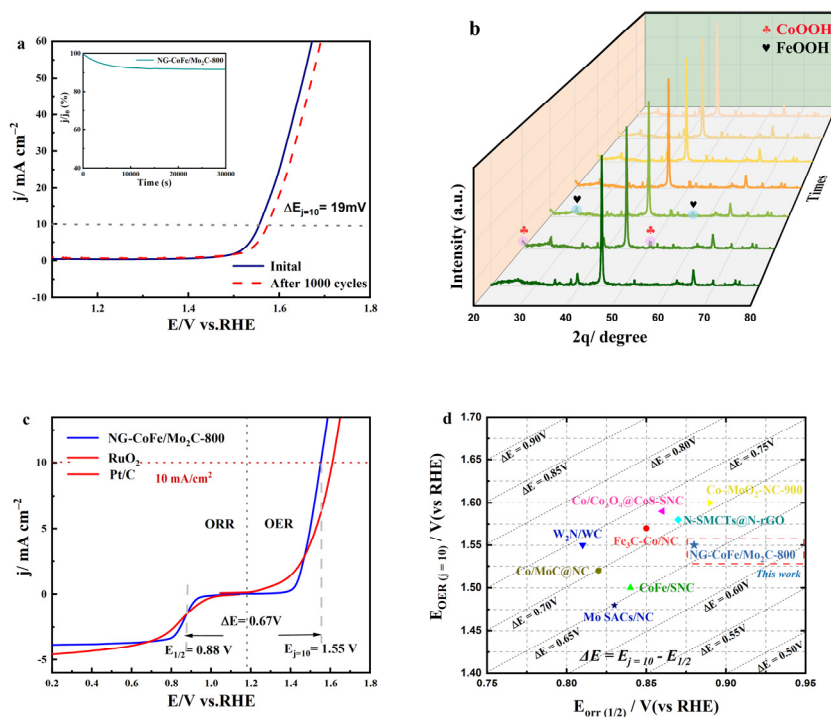


Figure 11. (a) OER polarization curves of NG-CoFe/Mo₂C-800 before and after the continuous operation in 1 M KOH at 1600 rpm, and the inset shows chronoamperometric responses (current-time (i-t)) of NG-CoFe/Mo₂C-800; (b) in situ XRD patterns of NG-CoFe/Mo₂C-800 collected during OER. (c) polarization curves of NG-CoFe/Mo₂C-800 and Pt/C (or RuO₂) catalysts using the three-electrode system in the full ORR/OER region in O₂-saturated 0.1 M KOH solution; (d) ORR and OER activities of NG-CoFe/Mo₂C-800 compared with those of representative electrocatalysts in the literature (ΔE represents the difference).

The ORR and OER mechanisms on NG-CoFe/Mo₂C-800 in alkaline media are speculated in Figure 12. For ORR, the synergistic interactions among FeCo and Mo₂C are mainly responsible for the high activity [75,76]. Among them, the Mo₂C particles provide abundant active sites for ORR [38], and the ultrathin N-doped carbon layer coated on the alloy surface enhances the electron transfer efficiency. According to previous reports, the introduction of Mo₂C can significantly reduce the dissociation potential of O₂* and

accelerate the ORR process [38,77]. Moreover, the interaction between Mo_2C and CoFe provides a large contribution for facilitating the formation of intermediates (O^* and $^*\text{OH}$), thus enhancing the ORR activity of NG-CoFe/ Mo_2C -800 [42,78,79]. For OER, the structural interaction between CoFe and Mo_2C should lead to the charge rearrangement, which helps to create more active sites (with active CoOOH/FeOOH species) on CoFe alloys and facilitates the smooth electron transfer process, thus enhancing the electrocatalytic activity [79,80]. Moreover, the porous structure of NG-CoFe/ Mo_2C -800 allows the electrolyte to make full contact with the catalyst, improving the mass transfer efficiency for ORR/OER [74,81]. Meanwhile, the graphitic carbon layer with excellent electrical conductivity protects the internal alloys/ Mo_2C from corrosion in harsh conditions, improving the ORR/OER catalytic stability [82–85].

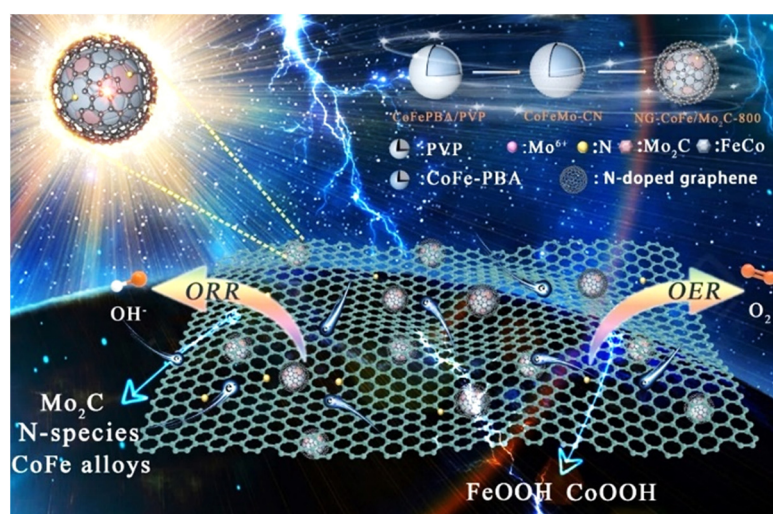


Figure 12. Schematic illustration of ORR/OER mechanisms on the NG-CoFe/ Mo_2C -800 catalyst in alkaline media.

4. Conclusions

In summary, by using CoFePBA/PVP as a precursor, we successfully synthesize a composite electrocatalyst (NG-CoFe/ Mo_2C -800) with CoFe alloy and Mo_2C nanoparticles encapsulated in an N-doped carbon skeleton to achieve a promising bifunctional (ORR/OER) activity ($\Delta E = 0.67$ V) in alkaline media. After 30,000 s of CA test (ORR), the current density of NG-CoFe/ Mo_2C -800 decreases by only 15.26% due to the presence of highly active metal species (Mo_2C and CoFe alloy) protected by N-doped carbon, and after 1000 LSV cycles (OER), approximately 91.8% of the current density is maintained due to the in-situ generation of hydroxyl oxides (CoOOH/FeOOH) originated from the CoFe alloys. Mo_2C doping plays an important role in modulating the carbon skeleton and FeCo alloy to form a unique CoFe/ Mo_2C -carbon encapsulated structure, which enhances the corrosion resistance of the catalyst (NG-CoFe/ Mo_2C -800) in harsh environments and maintains structural stability during the long-term ORR/OER cycles. This study provides a new strategy for the synthesis of carbon-coated metallic species, facilitating the development of efficient alloy/TMC-based electrocatalysts for bifunctional oxygen electrocatalysis.

Supplementary Materials: The following supporting information can be downloaded at: <https://www.mdpi.com/article/10.3390/nano13030543/s1>, Figure S1: High resolution XPS spectra of C 1s (a), N 1s (b), Fe 2p (c), Co 2p (d) and Mo 3d (e) for NG-CoFe/ Mo_2C -700; Figure S2: High resolution XPS spectra of C 1s (a), N 1s (b), Fe 2p (c), Co 2p (d) and Mo 3d (e) for NG-CoFe/ Mo_2C -750; Figure S3: High resolution XPS spectra of C 1s (a), N 1s (b), Fe 2p (c), Co 2p (d) and Mo 3d (e) for NG-CoFe/ Mo_2C -850; Figure S4: High resolution XPS spectra of C 1s (a), N 1s (b), Fe 2p (c), Co 2p (d) and Mo 3d (e) for NG-CoFe/ Mo_2C -900; Figure S5: Nyquist curves of NG-CoFe/ Mo_2C -x in an O_2 -saturated 0.1 M KOH solution at a scan rate of 5 mV s^{-1} with a rotation rate of 1600 rpm for ORR; The inset figure is the equivalent-circuit diagram. Figure S6: Electron-transfer number n derived from K-L plots at

different potentials; Figure S7: ORR polarization curves of NG-CoFe/Mo₂C-800 (a) and Pt/C (b) before and after the continuous CV tests in the O₂-saturated 0.1 M KOH at 1600 rpm; Figure S8: LSV curves of NG-CoFe/Mo₂C-x (x = 700, 750, 800, 850 and 900) in 1 M KOH solution for OER (2 mV s⁻¹ and 1600 rpm); Figure S9: Cyclic voltammograms with various scan rates from 40 to 120 mV s⁻¹ of NG-CoFe/Mo₂C-x [(x = 700 (a), 750 (b), 800 (c), 850 (d) and 900 (e)]; Figure S10: Area of redox features in CV curve of NG-CoFe/Mo₂C-800 (a), RuO₂ (b) for calculation of the number of surface-active sites; Figure S11: SEM images of NG-CoFe/Mo₂C-800 catalyst after ORR (a) and OER (b) stability tests; Table S1: Chemical compositions (wt. %) of NG-CoFe/Mo₂C-x electrocatalysts obtained from XPS analyses; Table S2: Textural properties of CoFePBA/PVP, CoFe-C and NG-CoFe/Mo₂C-800 composites. References [86–95] are cited in the supplementary materials.

Author Contributions: Synthesis, characterization, and original draft preparation, J.X. and Y.M.; investigation, resources, and data curation, B.L., S.S., X.Z., X.X. and C.H.; review, editing, and project administration, Y.Y., Z.S. and J.Z. All authors have read and agreed to the published version of the manuscript.

Funding: We acknowledge the support of the National Natural Science Foundation of China (52070074, 21806031 and 51578218), the Outstanding Youth Fund of Heilongjiang Province (JQ2022E005), and the Longjiang Scholars Program (Young Scholar, Q201912).

Institutional Review Board Statement: Not applicable.

Informed Consent Statement: Not applicable.

Data Availability Statement: Data can be made available upon request.

Acknowledgments: All authors thank the editors and anonymous reviewers for their valuable work.

Conflicts of Interest: The authors declare that they have no known competing financial interest or personal relationships that could have appeared to influence the work reported in this paper.

References

1. Gu, T.; Sa, R.; Zhang, L.; Li, D.; Wang, R. Engineering interfacial coupling between Mo₂C nanosheets and Co@NC polyhedron for boosting electrocatalytic water splitting and zinc-air batteries. *Appl. Catal. B* **2021**, *296*, 120360. [CrossRef]
2. Liu, C.; Tang, Y.; Wang, X.; Huang, W.; Li, S.; Dong, L.; Lan, Y. Highly active Co-Mo-C/NRGO composite as an efficient oxygen electrode for water-oxygen redox cycle. *J. Mater. Chem. A* **2016**, *4*, 18100–18106. [CrossRef]
3. Lian, Y.; Shi, K.; Yang, H.; Sun, H.; Qi, P.; Ye, J.; Wu, W.; Deng, Z.; Peng, Y. Elucidation of active sites on S, N codoped carbon cubes embedding Co-Fe carbides toward reversible oxygen conversion in high-performance zinc-air batteries. *Small* **2020**, *16*, 1907368. [CrossRef]
4. Lu, X.; Chen, Y.; Wang, S.; Gao, S.; Lou, X. Interfacing manganese oxide and cobalt in porous graphitic carbon polyhedrons boosts oxygen electrocatalysis for Zn-air batteries. *Adv. Mater.* **2019**, *31*, 1902339. [CrossRef]
5. Chai, G.; Qiu, K.; Qiao, M.; Titirici, M.; Shang, C.; Guo, Z. Active sites engineering leads to exceptional ORR and OER bifunctionality in P,N Co-doped graphene frameworks. *Energy Environ. Sci.* **2017**, *10*, 1186–1195. [CrossRef]
6. Cheng, W.; Yuan, P.; Lv, Z.; Guo, Y.; Qiao, Y.; Xue, X.; Liu, X.; Bai, W.; Wang, K.; Xu, Q.; et al. Boosting defective carbon by anchoring well-defined atomically dispersed metal-N₄ sites for ORR, OER, and Zn-air batteries. *Appl. Catal. B* **2020**, *260*, 118198. [CrossRef]
7. Li, M.; Zhu, Y.; Wang, H.; Wang, C.; Pinna, N.; Lu, X. Ni strongly coupled with Mo₂C encapsulated in nitrogen-doped carbon nanofibers as robust bifunctional catalyst for overall water splitting. *Adv. Energy Mater.* **2019**, *9*, 1803185. [CrossRef]
8. Kim, M.; Kim, S.; Song, D.; Oh, S.; Chang, K.; Cho, E. Promotion of electrochemical oxygen evolution reaction by chemical coupling of cobalt to molybdenum carbide. *Appl. Catal. B* **2018**, *227*, 340–348. [CrossRef]
9. Liang, Q.; Jin, H.; Wang, Z.; Xiong, Y.; Yuan, S.; Zeng, X.; He, D.; Mu, S. Metal-organic frameworks derived reverse-encapsulation Co-NC@Mo₂C complex for efficient overall water splitting. *Nano Energy* **2019**, *7*, 746–752. [CrossRef]
10. Peng, F.; Zhang, L.; Jiang, B.; Dou, H.; Xu, M.; Yang, N.; Zhang, J.; Sun, Y. In-situ synthesis of microflower composed of N-doped carbon films and Mo₂C coupled with Ni or FeNi alloy for water splitting. *Chem. Eng. J.* **2022**, *427*, 131712. [CrossRef]
11. Du, Q.; Zhao, R.; Guo, T.; Liu, L.; Chen, X.; Zhang, J.; Du, J.; Li, J.; Mai, L.; Asefa, T. Highly dispersed Mo₂C nanodots in carbon nanocages derived from Mo-based xerogel: Efficient electrocatalysts for hydrogen evolution. *Small Methods* **2021**, *5*, 2100334. [CrossRef] [PubMed]
12. Guo, Y.; Tang, J.; Henzie, J.; Jiang, B.; Qian, H.; Wang, Z.; Tan, H.; Bando, Y.; Yamauchi, Y. Assembly of hollow mesoporous nanoarchitectures composed of ultrafine Mo₂C nanoparticles on N-doped carbon nanosheets for efficient electrocatalytic reduction of oxygen. *Mater. Horiz.* **2017**, *4*, 1171–1177. [CrossRef]

13. Zhou, Z.; Yuan, Z.; Li, S.; Li, H.; Chen, J.; Wang, Y.; Huang, Q.; Wang, C.; Karahan, H.; Henkelman, G.; et al. Big to small: Ultrafine Mo₂C particles derived from giant polyoxomolybdate clusters for hydrogen evolution reaction. *Small* **2019**, *15*, 1900358. [[CrossRef](#)] [[PubMed](#)]
14. Hu, Q.; Liu, X.; Zhu, B.; Fan, L.; Chai, X.; Zhang, Q.; Liu, J.; He, C.; Lin, Z. Crafting MoC₂-doped bimetallic alloy nanoparticles encapsulated within N-doped graphene as roust bifunctional electrocatalysts for overall water splitting. *Nano Energy* **2018**, *50*, 212–219. [[CrossRef](#)]
15. Kou, Z.; Yu, Y.; Liu, X.; Gao, X.; Zheng, L.; Zou, H.; Pang, Y.; Wang, Z.; Pan, Z.; He, J.; et al. Potential-dependent phase transition and Mo-enriched surface reconstruction of γ -CoOOH in a heterostructured Co-Mo₂C precatalyst enable water oxidation. *ACS Catal.* **2020**, *10*, 4411–4419. [[CrossRef](#)]
16. Choi, J.; Lim, J.; Kim, D.; Park, S.; Yan, B.; Ko, D.; Cho, Y.; Lee, L.; Piao, Y. CoFe Prussian blue analogues on 3D porous N-doped carbon nanosheets boost the intercalation kinetics for a high-performance quasi-solid-state hybrid capacitor. *J. Mater. Chem. A* **2022**, *10*, 14501–14512. [[CrossRef](#)]
17. Zhan, T.; Liu, X.; Lu, S.; Hou, W. Nitrogen doped NiFe layered double hydroxide/reduced graphene oxide mesoporous nanosphere as an effective bifunctional electrocatalyst for oxygen reduction and evolution reactions. *Appl. Catal. B* **2017**, *205*, 551–558. [[CrossRef](#)]
18. Zheng, J.; Kang, T.; Liu, B.; Wang, P.; Li, H.; Yang, M. N-doped carbon nanotubes encapsulated with FeNi nanoparticles derived from defect-rich, molecule-doped 3D g-C₃N₄ as an efficient bifunctional electrocatalyst for rechargeable zinc–air batteries. *J. Mater. Chem. A* **2022**, *10*, 9911–9921. [[CrossRef](#)]
19. Liang, X.; Wang, G.; Gu, W.; Ji, G. Prussian blue analogue derived carbon-based composites toward lightweight microwave absorption. *Carbon* **2021**, *177*, 97–106. [[CrossRef](#)]
20. Yuan, S.; Xia, M.; Liu, Z.; Wang, K.; Xiang, L.; Huang, G.; Zhang, J.; Li, N. Dual synergistic effects between Co and Mo₂C in Co/Mo₂C heterostructure for electrocatalytic overall water splitting. *Chem. Eng. J.* **2022**, *430*, 132697. [[CrossRef](#)]
21. Zhu, Q.; Xu, S.; Harris, M.; Ma, C.; Liu, Y.; Wei, X.; Xu, H.; Zhou, Y.; Cao, Y.; Wang, K.; et al. A composite of carbon-wrapped Mo₂C nanoparticle and carbon nanotube formed directly on Ni foam as a high-performance binder-free cathode for Li–O₂ batteries. *Adv. Funct. Mater.* **2016**, *26*, 8514–8520. [[CrossRef](#)]
22. Qiu, H.; Du, P.; Hu, K.; Gao, J.; Li, H.; Liu, P.; Lna, T.; Ohara, K.; Ito, Y.; Chen, M. Metal and nonmetal codoped 3D nanoporous graphene for efficient bifunctional electrocatalysis and rechargeable Zn–air batteries. *Adv. Mater.* **2019**, *31*, 1900843. [[CrossRef](#)]
23. Huang, T.; Niu, Y.; Yang, Q.; Yang, W.; Xu, M. Self-template synthesis of prussian blue analogue hollow polyhedrons as superior sodium storage cathodes. *ACS Appl. Mater. Interfaces* **2021**, *13*, 37187–37193. [[CrossRef](#)] [[PubMed](#)]
24. Wang, J.; Yang, B.; Peng, X.; Ding, Y.; Yu, S.; Zhang, F.; Zhang, L.; Wu, H.; Guo, J. Design and preparation of polyoxometalate-based catalyst [MIMPs]₃PMo₆W₆O₄₀ and its application in deep oxidative desulfurization with excellent recycle performance and low molar O/S ratio. *Chem. Eng. J.* **2022**, *429*, 132446. [[CrossRef](#)]
25. Pendashteh, A.; Palma, J.; Anderson, M.; Marcilla, R. NiCoMnO₄ nanoparticles on N-doped graphene: Highly efficient bifunctional electrocatalyst for oxygen reduction/evolution reactions. *Appl. Catal. B* **2017**, *201*, 241–252. [[CrossRef](#)]
26. Yang, C.; Zai, S.; Zhou, Y.; Du, L.; Jiang, Q. Fe₃C–Co nanoparticles encapsulated in a hierarchical structure of N-doped carbon as a multifunctional electrocatalyst for ORR, OER, and HER. *Adv. Funct. Mater.* **2019**, *29*, 1901949. [[CrossRef](#)]
27. Amiin, I.; Liu, X.; Pu, Z.; Li, W.; Li, Q.; Zhang, J.; Tang, H.; Zhang, H.; Mu, S. From 3D ZIF nanocrystals to Co–N_x/C nanorod array electrocatalysts for ORR, OER, and Zn–air batteries. *Adv. Funct. Mater.* **2018**, *28*, 1704638. [[CrossRef](#)]
28. Marshall-Roth, T.; Libretto, N.; Wrobel, A.; Anderton, K.; Pegis, M.; Ricke, N.; Voorhis, T.; Miller, J.; Surendranath, Y. A pyridinic Fe–N₄ macrocycle models the active sites in Fe/N-doped carbon electrocatalysts. *Nat. Commun.* **2020**, *11*, 5283. [[CrossRef](#)] [[PubMed](#)]
29. Karuppanan, M.; Kim, Y.; Sung, Y.; Kwon, O. Nitrogen-rich hollow carbon spheres decorated with FeCo/fluorine-rich carbon for high performance symmetric supercapacitors. *J. Mater. Chem. A* **2018**, *6*, 7522–7531. [[CrossRef](#)]
30. Xu, F.; Wang, J.; Zhang, Y.; Wang, W.; Guan, T.; Wang, N.; Li, K. Structure-engineered bifunctional oxygen electrocatalysts with Ni₃S₂ quantum dot embedded S/N-doped carbon nanosheets for rechargeable Zn–air batteries. *Chem. Eng. J.* **2022**, *432*, 134256. [[CrossRef](#)]
31. Rossmeisl, J.; Logadottir, A.; Nørskov, J.K. Electrolysis of water on (oxidized) metal surfaces. *Chem. Phys.* **2005**, *319*, 178–184. [[CrossRef](#)]
32. Das, D.; Santra, S.; Nanda, K. In situ fabrication of a nickel/molybdenum carbide-anchored N-doped graphene/CNT hybrid: An efficient (pre)catalyst for OER and HER. *ACS Appl. Mater. Interfaces* **2018**, *10*, 35025–35038. [[CrossRef](#)]
33. Mo, Y.; Lin, J.; Li, S.; Yu, J. Anchoring Mo₂C nanoparticles on vertical graphene nanosheets as a highly efficient catalytic interlayer for Li–S batteries. *Chem. Eng. J.* **2022**, *433*, 134306. [[CrossRef](#)]
34. Li, G.; Tang, Y.; Fu, T.; Xiang, Y.; Xiong, Z.; Si, Y.; Guo, C.; Jiang, Z.S. N co-doped carbon nanotubes coupled with CoFe nanoparticles as an efficient bifunctional ORR/OER electrocatalyst for rechargeable Zn–air batteries. *Chem. Eng. J.* **2022**, *429*, 132174. [[CrossRef](#)]
35. Yu, Y.; You, S.; Du, J.; Zhang, P.; Dai, Y.; Liu, M.; Jiang, B.; Ren, N.; Zou, J. Ti³⁺-self-doped TiO₂ with multiple crystal-phases anchored on acid-pickled ZIF-67-derived Co₃O₄@N-doped graphitized-carbon as a durable catalyst for oxygen reduction in alkaline and acid media. *Chem. Eng. J.* **2021**, *403*, 1385–8947. [[CrossRef](#)]

36. Li, Y.; Li, J.; Dai, Y.; Li, X.; Shao, C.; Sun, Y.; Wang, R.; Zou, J. Co₃O₄@carbon with high Co²⁺/Co³⁺ ratios derived from ZIF-67 supported on N-doped carbon nanospheres as stable bifunctional oxygen catalysts. *Mater. Today Energy* **2021**, *21*, 100737. [[CrossRef](#)]
37. Fan, X.; Liu, Y.; Peng, Z.; Zhang, Z.; Zhou, H.; Zhang, X.; Yakobson, B.; Goddard, W.; Guo, X.; Hauge, R.; et al. Atomic H-induced Mo₂C hybrid as an active and stable bifunctional electrocatalyst. *ACS Nano* **2017**, *11*, 384–394. [[CrossRef](#)]
38. Luo, Y.; Wang, Z.; Fu, Y.; Jin, C.; Wei, Q.; Yang, R. In situ preparation of hollow Mo₂C–C hybrid microspheres as bifunctional electrocatalysts for oxygen reduction and evolution reactions. *J. Mater. Chem. A* **2016**, *4*, 12583–12590. [[CrossRef](#)]
39. Liu, Y.; Luo, X.; Zhou, C.; Du, S.; Zhen, D.; Chen, B.; Li, J.; Wu, Q.; Lru, Y.; Chen, D. A modulated electronic state strategy designed to integrate active HER and OER components as hybrid heterostructures for efficient overall water splitting. *Appl. Catal. B* **2020**, *260*, 118197. [[CrossRef](#)]
40. Shah, S.; Paidi, V.; Jung, H.; Kim, S.; Lee, G.; Han, J.; Lee, K.; Park, J. Unprecedented electrocatalytic oxygen evolution performances by cobalt-incorporated molybdenum carbide microflowers with controlled charge re-distribution. *J. Mater. Chem. A* **2021**, *9*, 1770–1783. [[CrossRef](#)]
41. Regmi, Y.; Waetzig, G.; Duffee, K.; Schmuecker, S.; Thode, J.; Leonard, B. Carbides of group IVA, VA and VIA transition metals as alternative HER and ORR catalysts and support materials. *J. Mater. Chem. A* **2015**, *3*, 10085–10091. [[CrossRef](#)]
42. Zhang, L.; Yang, T.; Zang, W.; Kou, Z.; Ma, Y.; Waqar, M.; Liu, X.; Zheng, L.; Pennycook, S.; Liu, Z.; et al. Quasi-paired Pt atomic sites on Mo₂C promoting selective four-electron oxygen reduction. *Adv. Sci.* **2021**, *8*, 2101344. [[CrossRef](#)] [[PubMed](#)]
43. Zhao, M.; Liu, H.; Zhang, H.; Chen, W.; Sun, H.; Wang, Z.; Zhang, B.; Song, L.; Yang, Y.; Ma, C.; et al. A pH-universal ORR catalyst with single-atom iron sites derived from a double-layer MOF for superior flexible quasi-solid-state rechargeable Zn–air batteries. *Energy Environ. Sci.* **2021**, *14*, 6455–6463. [[CrossRef](#)]
44. Wei, H.; Xi, Q.; Chen, X.; Guo, D.; Ding, F.; Yang, Z.; Wang, S.; Li, J.; Huang, S. Molybdenum carbide nanoparticles coated into the graphene wrapping N-doped porous carbon microspheres for highly efficient electrocatalytic hydrogen evolution both in acidic and alkaline media. *Adv. Sci.* **2018**, *5*, 1700733. [[CrossRef](#)]
45. Li, Y.; Gao, J.; Zhang, F.; Qian, Q.; Liu, Y.; Zhang, G. Hierarchical 3D macrosheets composed of interconnected in situ cobalt catalyzed nitrogen doped carbon nanotubes as superior bifunctional oxygen electrocatalysts for rechargeable Zn–air batteries. *J. Mater. Chem. A* **2018**, *6*, 15523–15529. [[CrossRef](#)]
46. Wang, Z.; Luo, H.; Lin, R.; Lei, H.; Yuan, Y.; Zhu, Z.; Li, X.; Mai, W. Theoretical calculation guided electrocatalysts design: Nitrogen saturated porous Mo₂C nanostructures for hydrogen production. *Appl. Catal. B* **2019**, *257*, 117891. [[CrossRef](#)]
47. Du, C.; Huang, H.; Wu, Y.; Wu, S.; Song, W. Ultra-efficient electrocatalytic hydrogen evolution at one-step carbonization generated molybdenum carbide nanosheets/N-doped carbon. *Nanoscale* **2016**, *8*, 16251–16258. [[CrossRef](#)]
48. Zhao, Y.; Wu, H.; Wang, Y.; Liu, L.; Qin, W.; Liu, S.; Liu, J.; Qin, Y.; Zhang, D.; Chu, A.; et al. Sulfur coordination engineering of molybdenum single-atom for dual-functional oxygen reduction/evolution catalysis. *Energy Storage Mater.* **2022**, *50*, 186–195. [[CrossRef](#)]
49. Chen, B.; He, X.; Yin, F.; Wang, H.; Liu, D.; Shi, R.; Chen, J.; Yin, H. MO-Co@N-doped carbon (M = Zn or Co): Vital roles of inactive Zn and highly efficient activity toward oxygen reduction/evolution reactions for rechargeable Zn-air battery. *Adv. Funct. Mater.* **2017**, *27*, 1700795. [[CrossRef](#)]
50. Zhu, Z.; Yin, H.; Wang, Y.; Chuang, C.; Xing, L.; Dong, M.; Lu, Y.; Casillas-Garcia, G.; Zheng, Y.; Chen, S.; et al. Coexisting single-atomic Fe and Ni sites on hierarchically ordered porous carbon as a highly efficient ORR electrocatalyst. *Adv. Mater.* **2020**, *32*, 2004670. [[CrossRef](#)]
51. Tavakkoli, M.; Flahaut, E.; Peljo, P.; Sainio, J.; Davodi, F.; Lobiak, E.; Mustonen, K.; Kauppinen, E. Mesoporous single-atom-doped graphene–carbon nanotube hybrid: Synthesis and tunable electrocatalytic activity for oxygen evolution and reduction reactions. *ACS Catal.* **2020**, *10*, 4647–4658. [[CrossRef](#)]
52. Ahn, C.; Yang, W.; Kim, J.; Priyanga, G.; Thomas, T.; Deshpande, N.; Lee, H.; Cho, H. Design of hydrangea-type Co/Mo bimetal MOFs and MOF-derived Co/Mo₂C embedded carbon composites for highly efficient oxygen evolution reaction. *Chem. Eng. J.* **2022**, *435*, 134815. [[CrossRef](#)]
53. Lee, J.H.; Kattel, S.; Wang, Y.; Tackett, B.M.; Xie, Z.; Hwang, S.; Denny, S.R.; Xu, W.; Chen, J.G. Prussian blue analogues as platform materials for understanding and developing oxygen evolution reaction electrocatalysts. *Chin. J. Catal.* **2021**, *393*, 390–398. [[CrossRef](#)]
54. Ouyang, T.; Ye, Y.; Wu, C.; Xiao, K.; Liu, Z. Heterostructures composed of N-doped carbon nanotubes encapsulating cobalt and beta-Mo₂C nanoparticles as bifunctional electrodes for water splitting. *Angew. Chem. Int. Ed.* **2019**, *58*, 4923–4928. [[CrossRef](#)]
55. Wu, X.; He, S.; Kong, Q.; An, X.; Yao, W.; Feng, W.; Wang, Q.; Qian, L.; Xiang, Z. Urchin-like Fe_xCo_{1-x}/CoOOH/FeOOH nanoparticles for highly efficient oxygen evolution reaction. *Appl. Surf. Sci.* **2022**, *577*, 151830. [[CrossRef](#)]
56. Wang, T.; Long, X.; Wei, S.; Wang, P.; Wang, C.; Jin, J.; Hu, G. Boosting hole transfer in the fluorine-doped hematite photoanode by depositing ultrathin amorphous FeOOH/CoOOH cocatalysts. *ACS Appl. Mater. Interfaces* **2020**, *12*, 49705–49712. [[CrossRef](#)]
57. Yin, X.; Dai, X.; Nie, F.; Gan, Y.; Ye, Y.; Ren, Z.; Liu, Y.; Wu, B.; Cao, Y.; Zhang, X. Electronic modulation and surface reconstruction of cactus-like CoB₂O₄@FeOOH heterojunctions for synergistically triggering oxygen evolution reactions. *J. Mater. Chem. A* **2022**, *10*, 11386–11393. [[CrossRef](#)]
58. Li, F.; Ai, H.; Liu, D.; Lo, K.; Pan, H. An enhanced oxygen evolution reaction on 2D CoOOH via strain engineering: An insightful view from spin state transition. *J. Mater. Chem. A* **2021**, *9*, 17749–17759. [[CrossRef](#)]

59. Cheng, H.; Zhuang, Y.; Meng, C.; Chen, B.; Chen, J.; Yuan, A.; Zhou, H. Ultrafine CoFe nanoparticles supported on nitrogen-doped carbon sheets boost oxygen electrocatalysis for Zn-air batteries. *Appl. Surf. Sci.* **2023**, *607*, 154953. [[CrossRef](#)]
60. Han, N.; Luo, S.; Deng, C.; Zhu, S.; Xu, Q.; Min, Y. Defect-rich FeN_{0.023}/Mo₂C heterostructure as a highly efficient bifunctional catalyst for overall water-splitting. *ACS Appl. Mater. Interfaces* **2021**, *13*, 8306–8314. [[CrossRef](#)]
61. Chen, J.; Zheng, F.; Zhang, S.; Fisher, A.; Zhou, Y.; Wang, Z.; Li, Y.; Xu, B.; Li, J.; Sun, S. Interfacial interaction between FeOOH and Ni-Fe LDH to modulate the local electronic structure for enhanced OER electrocatalysis. *ACS Catal.* **2018**, *8*, 11342–11351. [[CrossRef](#)]
62. Ma, X.; Chai, H.; Cao, Y.; Xu, J.; Wang, Y.; Dong, H.; Jia, D.; Zhou, W. An effective bifunctional electrocatalysts: Controlled growth of CoFe alloy nanoparticles supported on N-doped carbon nanotubes. *J. Colloid Interface Sci.* **2018**, *514*, 656–663. [[CrossRef](#)]
63. Feng, J.; Xu, H.; Dong, Y.; Ye, S.; Tong, Y.; Li, G. FeOOH/Co/FeOOH hybrid nanotube arrays as high-performance electrocatalysts for the oxygen evolution reaction. *Angew Chem. Int. Ed.* **2016**, *55*, 3694–3698. [[CrossRef](#)]
64. Chen, Z.; Kronawitter, C.; Yeh, Y.; Yang, X.; Zhao, P.; Yao, N.; Koel, B. Activity of pure and transition metal-modified CoOOH for the oxygen evolution reaction in an alkaline medium. *J. Mater. Chem. A* **2017**, *5*, 842–850. [[CrossRef](#)]
65. Ye, S.; Wang, J.; Hu, J.; Chen, Z.; Zheng, L.; Fu, Y.; Lei, Y.; Ren, X.; He, C.; Zhang, Q.; et al. Electrochemical construction of low-crystalline CoOOH nanosheets with short-range ordered grains to improve oxygen evolution activity. *ACS Catal.* **2021**, *11*, 6104–6112. [[CrossRef](#)]
66. Anantharaj, S.; Kundu, S.; Noda, S. “The Fe effect”: A review unveiling the critical roles of Fe in enhancing OER activity of Ni and Co based catalysts. *Nano Energy* **2021**, *80*, 105514. [[CrossRef](#)]
67. Du, P.; Hu, K.; Lyu, J.; Li, H.; Lin, X.; Xie, G.; Liu, X.; Ito, Y.; Qiu, H. Anchoring Mo single atoms/clusters and N on edge-rich nanoporous holey graphene as bifunctional air electrode in Zn–air batteries. *Appl. Catal. B* **2020**, *276*, 119172. [[CrossRef](#)]
68. Tang, L.; Yu, L.; Ma, C.; Song, Y.; Tu, Y.; Zhang, Y.; Bo, X.; Deng, D. Three-dimensional CoOOH nanoframes confining high-density Mo single atoms for large-current-density oxygen evolution. *J. Mater. Chem. A* **2022**, *10*, 6242–6250. [[CrossRef](#)]
69. Niu, J.; Shao, R.; Liang, J.; Dou, M.; Li, Z.; Huang, Y.; Wang, F. Biomass-derived mesopore-dominant porous carbons with large specific surface area and high defect density as high-performance electrode materials for Li-ion batteries and supercapacitors. *Nano Energy* **2017**, *36*, 322–330. [[CrossRef](#)]
70. Ji, S.M.; Muthurasu, A.; Chhetri, K.; Kim, H.Y. Metal-organic framework assisted vanadium oxide nanorods as efficient electrode materials for water oxidation. *J. Colloid Interface Sci.* **2022**, *618*, 475–482. [[CrossRef](#)]
71. Chhetri, K.; Dahal, B.; Mukhiya, T.; Tiwari, A.P.; Muthurasu, A.; Kim, T.; Kim, H.; Kim, H.Y. Integrated hybrid of graphitic carbon-encapsulated Cu_xO on multilayered mesoporous carbon from copper MOFs and polyaniline for asymmetric supercapacitor and oxygen reduction reactions. *Carbon* **2021**, *179*, 89–99. [[CrossRef](#)]
72. Diao, J.; Li, X.; Wang, S.; Zhao, Z.; Wang, W.; Chen, K.; Chen, X.; Chao, T.; Yang, Y. Promoting water splitting on arrayed molybdenum carbide nanosheets with electronic modulation. *J. Mater. Chem. A* **2021**, *9*, 21440–21447. [[CrossRef](#)]
73. Hu, X.; Huang, L.; Zhang, J.; Li, H.; Zha, K.; Shi, L.; Zhang, D. Facile and template-free fabrication of mesoporous 3D nanosphere-like Mn_xCo_{3-x}O₄ as highly effective catalysts for low temperature SCR of NO_x with NH₃. *J. Mater. Chem. A* **2018**, *6*, 2952–2963. [[CrossRef](#)]
74. Kandel, M.R.; Pan, U.N.; Paudel, D.R.; Dhakal, P.P.; Kim, N.H.; Lee, J.H. Hybridized bimetallic phosphides of Ni–Mo, Co–Mo, and Co–Ni in a single ultrathin-3D-nanosheets for efficient HER and OER in alkaline media. *Compos. Part B* **2022**, *239*, 109992. [[CrossRef](#)]
75. Cheng, Z.; Fu, Q.; Han, Q.; Xiao, Y.; Liang, Y.; Zhao, Y.; Qu, L. A type of 1 nm molybdenum carbide confined within carbon nanomesh as highly efficient bifunctional electrocatalyst. *Adv. Funct. Mater.* **2018**, *28*, 1705967. [[CrossRef](#)]
76. Pintado, S.; Goberna-Ferrón, S.; Escudero-Adán, E.C.; Galán-Mascarós, J.R. Fast and Persistent Electrocatalytic Water Oxidation by Co–Fe Prussian Blue Coordination Polymers. *J. Am. Chem. Soc.* **2013**, *135*, 13270–13273. [[CrossRef](#)]
77. Liu, Y.; Yu, G.; Li, G.; Sun, Y.; Asefa, T.; Chen, W.; Zou, X. Coupling Mo₂C with nitrogen-rich nanocarbon leads to efficient hydrogen-evolution electrocatalytic sites. *Angew Chem. Int. Ed.* **2015**, *54*, 10752–10757. [[CrossRef](#)] [[PubMed](#)]
78. Hu, E.; Ning, J.; He, B.; Li, Z.; Zheng, C.; Zhong, Y.; Zhang, Z.; Hu, Y. Unusual formation of tetragonal microstructures from nitrogen-doped carbon nanocapsules with cobalt nanocores as a bi-functional oxygen electrocatalyst. *J. Mater. Chem. A* **2017**, *5*, 2271–2279. [[CrossRef](#)]
79. Liu, W.; Hu, X.; Li, H.; Yu, H. Pseudocapacitive Ni-Co-Fe hydroxides/N-doped carbon nanoplates-based electrocatalyst for efficient oxygen evolution. *Small* **2018**, *14*, 1801878. [[CrossRef](#)]
80. Fan, R.; Zhou, Y.; Li, M.; Xie, J.; Yu, W.; Chi, J.; Wang, L.; Yu, J.; Chai, Y.; Dong, B. In situ construction of Fe(Co)OOH through ultra-fast electrochemical activation as real catalytic species for enhanced water oxidation. *Chem. Eng. J.* **2021**, *426*, 131943. [[CrossRef](#)]
81. Lee, S.; Kim, J.; Chung, D.; Yoo, J.; Lee, H.; Kim, M.; Mun, B.; Kwon, S.; Sung, Y.; Hyeon, T. Design principle of Fe-N-C electrocatalysts: How to optimize multimodal porous structures? *J. Am. Chem. Soc.* **2019**, *141*, 2035–2045. [[CrossRef](#)]
82. Liang, B.; Yue, L.; Li, T.; Liu, Q.; Liu, Y.; Gao, S.; Alshehri, A.; Alzahrani, K.; Luo, Y.; Sun, X. CoFe-LDH nanowire arrays on graphite felt: A high-performance oxygen evolution electrocatalyst in alkaline media. *Chin. Chem. Lett.* **2022**, *33*, 890–892.
83. Lu, F.; Fan, K.; Cui, L.; Li, B.; Yang, Y.; Zong, L.; Wang, L. Engineering FeN₄ active sites onto nitrogen-rich carbon with tubular channels for enhanced oxygen reduction reaction performance. *Appl. Catal. B* **2022**, *313*, 121464. [[CrossRef](#)]

84. Liu, L.; Zeng, G.; Chen, J.; Bi, L.; Dai, L.; Wen, Z. N-doped porous carbon nanosheets as pH-universal ORR electrocatalyst in various fuel cell devices. *Nano Energy* **2018**, *49*, 393–402. [[CrossRef](#)]
85. Guo, M.; Xu, M.; Qu, Y.; Hu, C.; Yan, P.; Isimjan, T.; Yang, X. Electronic/mass transport increased hollow porous Cu₃P/MoP nanospheres with strong electronic interaction for promoting oxygen reduction in Zn-air batteries. *Appl. Catal. B* **2021**, *297*, 120415. [[CrossRef](#)]
86. Guo, Y.; Yuan, P.; Zhang, J.; Xia, H.; Cheng, F.; Zhou, M.; Li, J.; Qiao, Y.; Mu, S.; Xu, Q. Co₂P-CoN double active centers confined in N-doped carbon nanotube: Heterostructural engineering for trifunctional catalysis toward HER, ORR, OER, and Zn-air batteries driven water splitting. *Adv. Funct. Mater.* **2018**, *28*, 1805641. [[CrossRef](#)]
87. Jian, H.; Gu, J.; Zheng, X.; Liu, M.; Qiu, X.; Wang, L.; Li, W.; Chen, Z.; Ji, X.; Li, J. Defect-rich and ultrathin N doped carbon nanosheets as advanced trifunctional metal-free electrocatalysts for the ORR, OER and HER. *Energy Environ. Sci.* **2019**, *12*, 322–333. [[CrossRef](#)]
88. Zhong, H.; Li, K.; Zhang, Q.; Wang, J.; Meng, F.; Wu, Z.; Yan, J.; Zhang, X. In situ anchoring of Co₉S₈ nanoparticles on N and S Co-doped porous carbon tube as bifunctional oxygen electrocatalysts. *NPG Asia Mater.* **2016**, *8*, 308. [[CrossRef](#)]
89. Sun, T.; Wang, J.; Qiu, C.; Ling, X.; Tian, B.; Chen, W.; Su, C.B. N codoped and defect-rich nanocarbon material as a metal-free bifunctional electrocatalyst for oxygen reduction and evolution reactions. *Adv. Sci.* **2018**, *5*, 1800036. [[CrossRef](#)] [[PubMed](#)]
90. Guo, L.; Deng, J.; Wang, G.; Hao, Y.; Bi, K.; Wang, X.; Yang, Y. N, P-doped CoS₂ embedded in TiO₂ nanoporous films for Zn-air batteries. *Adv. Funct. Mater.* **2018**, *28*, 1804540. [[CrossRef](#)]
91. Zhang, R.; Zhang, C.; Chen, W. FeP embedded in N, P dual-doped porous carbon nanosheets: An efficient and durable bifunctional catalyst for oxygen reduction and evolution reactions. *J. Mater. Chem. A* **2016**, *4*, 18723–18729. [[CrossRef](#)]
92. Anantharaj, S.; Karthik, P.; Kundu, S. Self-assembled IrO₂ nanoparticles on a DNA scaffold with enhanced catalytic and oxygen evolution reaction (OER) activities. *J. Mater. Chem. A* **2015**, *3*, 24463–24478. [[CrossRef](#)]
93. Lee, S.; Bai, L.; Hu, X. Deciphering iron-dependent activity in oxygen evolution catalyzed by nickel-iron layered double hydroxide. *Angew Chem. Int. Ed.* **2020**, *59*, 8072–8077. [[CrossRef](#)] [[PubMed](#)]
94. Kuang, M.; Wang, Y.; Fang, W.; Tan, H.; Chen, M.; Yao, J.; Liu, C.; Xu, J.; Zhou, K.; Yan, Q. Efficient nitrate synthesis via ambient nitrogen oxidation with Ru-doped TiO₂ /RuO₂ electrocatalysts. *Adv. Mater.* **2020**, *32*, 2002189. [[CrossRef](#)] [[PubMed](#)]
95. Ren, J.; Chen, L.; Liu, Y.; Yuan, Z. Hollow cobalt phosphate microspheres for sustainable electrochemical ammonia production through rechargeable Zn–N₂ batteries. *J. Mater. Chem. A* **2021**, *9*, 11370–11380. [[CrossRef](#)]

Disclaimer/Publisher’s Note: The statements, opinions and data contained in all publications are solely those of the individual author(s) and contributor(s) and not of MDPI and/or the editor(s). MDPI and/or the editor(s) disclaim responsibility for any injury to people or property resulting from any ideas, methods, instructions or products referred to in the content.